

Unexpected fault activation in underground gas storage. Part II: Definition of safe operational bandwidths

Selena Baldan^{a,*}, Massimiliano Ferronato^a, Andrea Franceschini^a, Carlo Janna^a, Claudia Zoccarato^a, Matteo Frigo^b, Giovanni Isotton^b, Cristiano Collettini^c, Chiara Deangeli^d, Vera Rocca^d, Francesca Verga^d, Pietro Teatini^a

^a*Department of Civil, Environmental and Architectural Engineering, University of Padua, Padua, 35131 Italy*

^b*M3E S.r.l., Padua, 35121 Italy*

^c*Department of Earth Sciences, Sapienza University of Rome, Rome, 00185 Italy*

^d*Department of Environment, Land and Infrastructure Engineering, Politecnico di Torino, Turin, 10129 Italy*

Abstract

Underground gas storage is a versatile tool for managing energy resources and addressing pressing environmental concerns. While natural gas is stored in geological formations since the beginning of the 20th century, hydrogen has recently been considered as a potential candidate toward a more flexible and sustainable energy infrastructure. Furthermore, these formations can also be used to sequester environmentally harmful gases such as CO₂. When such operations are implemented in faulted basins, however, safety concerns may arise due to the possible reactivation of pre-existing faults, which could result in (micro)-seismicity events. In the Netherlands, it has been recently noted that fault reactivation can occur “unexpectedly” during the life of an underground gas storage (UGS) site, even when stress conditions are not expected to cause a failure. The present two-part work aims to develop a modeling framework to investigate the physical mechanisms causing such occurrences and define a safe operational bandwidth for pore pressure variation for UGS operations in the faulted reservoirs of the Rotliegend formation, the Netherlands. In this follow-up paper, we investigate in detail the mechanisms and crucial factors that result in fault reactivation at various stages of a UGS. The mathematical and numerical model described in Part I is used, also accounting for the effect of geochemical dissolution on reservoir and caprock weakening. The study investigates the risks of fault activation caused by the storage of different fluids for various purposes, such as long-term CO₂ sequestration, CH₄ and H₂ injection and extraction cycles, and N₂ injection as cushion gas. The results show how geological configuration, geomechanical properties, and reservoir operating conditions may increase the risk of fault reactivation at various UGS stages. Furthermore, the analysis indicates that reservoir pressure near critical levels and reactivation during primary production may significantly contribute to potential fault instabilities. In light of these findings, operational guidelines for improving secure and effective storage operations are thereby presented.

Keywords: Fault reactivation, Underground Gas Storage, Underground Hydrogen Storage, Carbon Capture and Sequestration, Safety guidelines

*Corresponding author

Email address: selena.baldan@phd.unipd.it (Selena Baldan)

1. Introduction

The development of underground gas storage sites has been crucial in the global energy infrastructure since the early 20th century. The first operational underground storage system (USS) site dates back to 1915 [1]. Over time, this technology has expanded with more than 600 facilities worldwide [16] to effectively manage gas supply and demand on both seasonal and daily bases [59]. While USS has typically focused on storing natural gas (i.e., mainly CH₄) through UGS, it possesses the potential to store a variety of gases for diverse purposes, thus becoming a flexible tool for managing energy resources and addressing environmental concerns. This is especially important as Europe moves toward a net-zero greenhouse gas emission energy system [15]. The scientific community has shown a growing interest in underground hydrogen storage (UHS) as an alternative to natural gas. Having the potential to accommodate significant volumes, ranging from tens of millions of cubic meters in caverns to potentially billions of cubic meters in depleted gas fields [20], hydrogen versatility and absence of carbon emissions during production and utilization make it a sustainable option. Additionally, carbon capture and storage (CCS) initiatives have identified underground storage of CO₂ as a crucial component in mitigating greenhouse gas emissions and contrasting climate change.

However, despite the widespread use of USS, one of the important aspects to be considered is the potential reactivation of existing faults and consequent induced seismicity [13, 16, 31]. Although such events are statistically rare [16], they demand significant attention due to their social and economic implications. In the Netherlands, natural gas is currently stored in four UGS facilities: Bergermeer, Alkmaar, Norg, and Grijpskerk. They are located in the Carboniferous-Rotliegend formation that widely extends in Central Europe and is considered one of the most extensively explored petroleum systems worldwide [19]. Over the past few decades, significant seismic activity associated to USS has been observed in this region [57, 55], particularly in three of the four UGS facilities (i.e., Bergermeer, Norg, and Grijpskerk). Excluding Castor [9, 60], Spain, and Hutubi [30, 34], China, cases, these Dutch reservoirs are the only cases where UGS activities have been definitively associated to induced seismicity events [60].

Recently, the Netherlands have also focused the attention on the feasibility of storing different gases in depleted gas fields and salt caverns as a crucial measure in the ongoing energy transition, by applying the same technology used in UGS to offshore CO₂ storage through the Porthos project [43], while research on hydrogen storage is in progress and primarily focused on salt caverns, although the potential for storage in abandoned gas fields is also being considered for the future. Additionally, besides being used as cushion gas [50], nitrogen is utilized to convert high-calorific gas to low-calorific gas for residential heating and cooking purposes in Dutch households. Currently, nitrogen is stored in a salt cavern near Heiligerlee [37, 39] for this purpose.

Given the future role that USS will play, it is crucial to understand why faults can become active and which mechanisms are potentially prone to lead to instability. During the cyclic or permanent storage of these fluids, fault reactivation can occur when the natural stress regime on a fault surface is altered due to changes in pore pressure within a reservoir. The interaction between human activities at depth and the existing stress conditions determine the initiation, amount of slip, and extent of fault reactivation [49, 25, 7].

Over a short- to mid-term timeframe (e.g., from days to years), fault reactivation can be interpreted through a geomechanical approach involving pressure variations following injection/extraction activities lasting decades. In this context, most human-induced seismic events can be easily explained, as they occur due to fluid injection causing pressure to rise beyond the initial level, ultimately leading the shear stress on the fracture surface to achieve its limit strength [61, 17]. However, a subset of recorded events cannot be accounted for by this mech-

anism. These events, identified as “unexpected” seismic events, occur when the pressure falls within the range already experienced during primary production. In this scenario, fault re-activation occurs not only during primary production or gas storage at pressures exceeding the initial value P_i [12, 9, 63], but also during gas injection or producing and storing phases with pore pressures below the initial value P_i but above P_{min} , which is the minimum pressure generally experienced by the reservoir at the end of primary production [21, 33, 54, 41]. A typical time-behavior of the fluid pressure variations expected in UGS and UHS applications is sketched in Figure 1. The recorded seismic events are unexpected because the stress state should have already been experienced by the reservoir and surrounding faults during previous production phases. Unraveling the underlying mechanisms behind these “unexpected” seismic events is crucial for ensuring the safe and efficient operation of underground gas storage facilities.

On the other hand, long-term processes, spanning hundreds or even thousands of years, primarily involve fluid-rock interactions that can alter fault rock fabric, mineralogy, frictional properties, and cohesion. Currently, the understanding of the specific impacts of different gases on the mechanical properties of faults and rock is still poorly understood, but the potential risk associated with their storage has to be considered. Indeed, the performance, efficiency, and safety of any storage greatly depends on fluid-rock interaction.

In this follow-up paper of [17], we conduct an investigation of the phenomenon of “unexpected” seismic events in underground gas storage facilities. By understanding the factors contributing to such events, we can establish enhanced guidelines and best practices for operating underground gas facilities during different storage phases. We present a comprehensive study to reassess the fundamental geomechanical causes of induced seismicity and specific risk factors, including the influence of geochemical dissolution effects on reservoir and caprock weakening.

This work has three specific aims. The first one is to improve the understanding of the physics-based processes behind the induced seismicity during both cycling and permanent gas storage. The second aim involves investigating which are the roles of the Rotliegend reservoirs peculiarities, i.e., the graben-fault bounds, and the compartmentalization into offset blocks by intra-field faults on favoring fault reactivation. Lastly, the third aim is to propose, based on the modeling outcomes, valuable insights into the development of general guidelines for safe operational bandwidths for reservoir storage conditions during pressure cycling (and noncycling) of underground storage of CH_4 , CO_2 , H_2 , and N_2 in depleted gas fields. These guidelines are intended to serve as a valuable tool, contributing to the effectiveness of risk assessment and mitigation strategies in underground gas storage operations. A few preliminary outcomes regarding UGS are already reported in [51, 52] and [17].

The analysis that follows is accomplished by using the mathematical and numerical framework developed in Part I of this work [17], where a Finite Element (FE) geomechanical simulator is implemented with a Lagrange multiplier-based treatment of the frictional contact conditions for reproducing the fault behavior. The simulator is supplemented also with visco-elasto-plastic constitutive laws [29], and fault activation is ruled by the Coulomb frictional criterion. Pressure change within the faults, variation of Coulomb’s parameters due to slip-weakening, and the rheology of the caprock are properly accounted for. Because of the main aims listed above, the modeling study is not focused on a specific UGS field, but on a conceptual reservoir and on a fault system that realistically represents the main geologic features of the Rotliegend formation system.

The paper is organized as follows. The typical setting of the Rotliegend reservoirs and a few examples of seismicity recorded during UGS are initially presented. Then, fluids under investigation are described, and the modeling set-up is outlined. The various scenarios are then

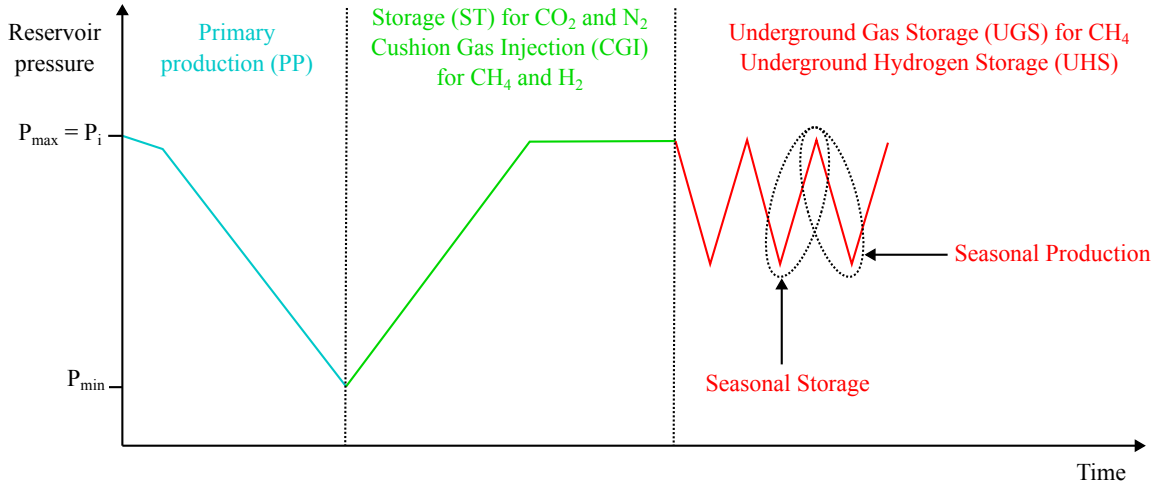


Figure 1: Sketch of the main stages during the reservoir lifespan in terms of pressure change over time for CH_4 , CO_2 , H_2 and N_2 : Primary Production (PP) for CH_4 production, Storage (ST) for CO_2 and N_2 storage, Cushion Gas Injection (CGI) for H_2 and CH_4 injection, and Underground H_2 Storage (UHS) and Underground Gas Storage (UGS) cycles for seasonal pressure fluctuations during CH_4/H_2 injection and withdrawal. Notice that, according to the Netherlands regulation, P must remain below P_i regardless of the stage under consideration.

developed to understand the geomechanical behavior of the faulted system, first analyzing the parameters involved in UGS and then comparing the scenarios using different fluids. Modeling results are presented, and the mechanisms responsible for fault reactivation during the different phases are identified. The modeling outcomes are discussed, highlighting the peculiarities of the storage scenarios with respect to induced seismicity during primary production as addressed in previous studies, ranking the natural features and anthropogenic factors prone to cause fault reactivation, and illustrating general operational guidelines to reduce the probability of reactivation occurrences.

2. Induced seismicity in Rotliegend UGS reservoirs

The Rotliegend formation stretches over a large region covering North-Western Germany, the Netherlands, with an off-shore portion that extends and includes part of the UK. The Rotliegend sandstones have been attributed to deposition in a variety of arid, terrestrial environments, among which ephemeral fluvial (wadi) systems, various types of eolian deposits, desert-lake environments, and adjacent sabkhas are dominant. The sealing nature of Zechstein salt is the main reason for the existence of the large amount of traps that sealed gas migrated from the underlying coals and carbonaceous shales of the Carboniferous Coal Measures for approximately 150 million years [19]. The Rotliegend unit spans a depth range between 2,000 and 4,700 m, and it is generally made of permeable sandstone (average 100-200 mD), with high net-to-gross and porosity (average 15-20%). The thickness of the reservoir sands is generally over 50 m and rarely exceeds 300 m. Faulting is the peculiarity of the geologic unit, with the majority of the faults that are Triassic-Tertiary features nucleated on Mid-Palaeozoic fault patterns and reworked during the Variscan orogeny. The Mesozoic rifting phase established the general extensional normal fault pattern [11].

As a consequence, many fields are formed by a number of rhomboid-shaped dipping fault blocks, positioned one next to each other. The trapping mechanism is structural, by the juxtaposition of the Rotliegend reservoir blocks against the thick evaporitic Zechstein formation. Moreover, the hydraulic connectivity between the various blocks is extremely poor, causing a clear compartmentalization of the reservoirs. Fault seal and, secondarily, stratigraphic barriers

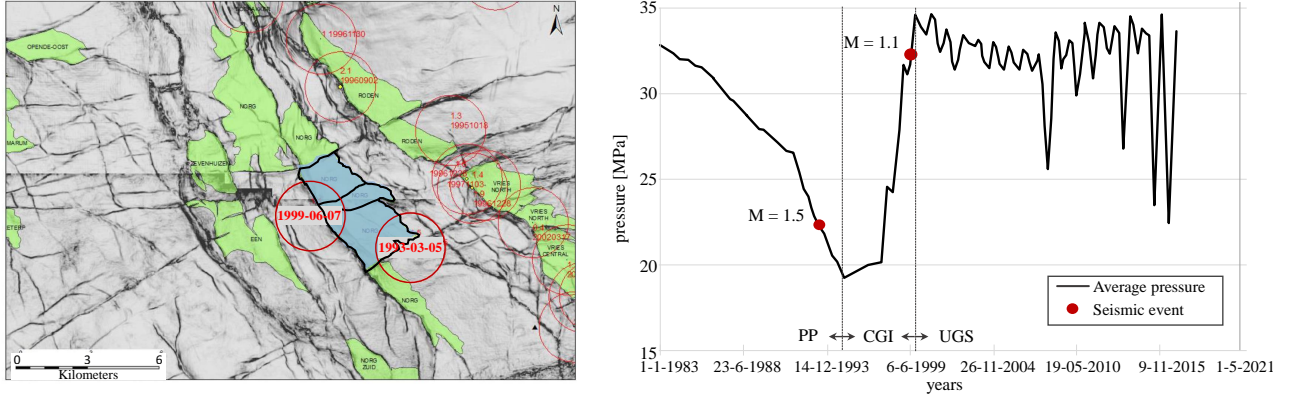


Figure 2: Left: Map of the Norg UGS site (in blue) with traces of the bounding faults (black lines) and localization of the recorded seismic events (red circles). Right: average pressure evolution over time at the Norg UGS field. The location of the two seismic events in 1993 and 1999 are reported (modified after [41]).

and diagenesis, are the causes of this compartmentalization [56]. The left frame in Figure 2 sketches as a representative examples the structural map of the Norg UGS reservoir.

The reservoir is bounded by normal faults with a significant (up to a 250 m) throw and consist of a few compartments also separated by internal faults. The gas fields are 2,500-3,500 m deep, with the Rotliegend reservoir rock characterized by an average net thickness of 150-200 m. As usual for UGS plants, the reservoir is a partially-depleted gas field that was converted to underground gas storage after a primary production (PP) period. PP is generally followed by a quick gas injection (CGI) phase when fluid pressure in the reservoir is risen to almost the original value, and then by the UGS injection and withdrawal cycles. Gas is injected at temperatures similar or slightly below those at the reservoir level, thus minimizing thermal stresses. The rightmost frame of Figure 2 summarizes the evolution of the average pressure in Norg. The timing and location of the seismic events recorded in the vicinity of the UGS reservoir is also shown in Figure 2. In Norg, the time of the first $M = 1.5$ earthquake coincided with low pressure level during PP. The second $M = 1.1$ seismic event occurred at the end of the CGI phase, with the pressure in the reservoir close to the original pressure level.

In Grijpskerk, where pressure differences over reservoir blocks can be as high as about 7 MPa, a first seismic event took place at the end of PP in 1997, and a second one much later, in 2015, almost at the end of a UGS production phase [54]. Four seismic events with a magnitude $M \in [3.0, 3.5]$ were detected in 1994 and 2001 during PP in the Bergermeer reservoir. The events were located at the tip of the central fault separating the two main blocks [54]. A down-hole micro-seismic array characterized by a magnitude of completeness below $M = 0$ was established during the CGI phase. The array recorded a large number of micro-seismic events ($M < 0$) on the faults at the reservoir depth and a main event with $M = 0.9$ along the central fault when the pressure difference between the two blocks peaked about 4 MPa at the beginning of 2013 [3].

3. Chemo-mechanical effects by CO_2 , H_2 and N_2 on rocks and faults

3.1. Effect on rock and caprock

The interactions between gas, brine, and rock can lead to significant changes in the reservoir and fault properties that, in turn, can greatly impact the performance, efficiency, and safety of the storage process.

However, the impact of injected gas type on the mechanical response of sedimentary rocks is still not well understood. Existing research predominantly focuses on CO₂ injection [32], with limited investigation into N₂ injection [26, 18]. There is some ongoing development regarding H₂ injection into sedimentary rocks [5, 58]. The latest comprehensive review on H₂ injection and withdrawal has been compiled by [38]. From the extensive available literature on CO₂-fluid-rock interactions, e.g., [46] and [42], two contrasting viewpoints emerge: CO₂ can either have a negligible influence on the rock mechanical parameters, or degrade them because of mineral dissolution and modifications in pore size distribution. A stable condition is often observed when the mineral composition and pore structure remain unchanged during CO₂ injection [45, 4], with the main elastic properties largely unaffected by the CO₂ presence [36, 26]. Conversely, in cases where a weakening effect is observed after CO₂ injection, the mechanical strength of the rock decreases, leading to increased permeability and reduced rock stiffness. The dissolution of carbonate minerals, particularly calcite, reduces the cohesion of the rock matrix and weakens grain-to-grain contacts [32]. This effect has been observed in experiments on sedimentary rocks like sandstones and carbonates. Generally, carbonate-rich rocks are more susceptible to mechanical weakening due to CO₂-fluid-rock interactions.

While several experimental evidences support these findings, uncertainties still persist in the results. For instance, CO₂-acidified brine injection can precipitate minerals, potentially increasing the strength and stiffness of the rock depending on the specific material and its mineral composition. CO₂ can react with certain minerals like calcite, inducing mineral precipitation and cementation, thereby enhancing the mechanical integrity of the rock [14]. Sandstones, for example, may experience both increase and decrease in the deformation moduli [35]. The variability in results regarding the effects on rock stiffness and strength highlights the need for additional experimental data to address existing uncertainties. Regarding the geochemical effects of CO₂ injection in the Upper Rotliegend formation, [4] reported an increase in permeability ranging from 10% to 30%. This suggests changes in porosity and deformation moduli, with potential deformation moduli variation of $\pm 30\%$ [22, 35].

Regarding N₂ and H₂ injection, there is a limited investigation. N₂ is primarily used for determining rock porosity and permeability or as a control gas [18]. Therefore, the exposure of rocks to N₂ is expected to have negligible effects, although further investigations are required. In the case of H₂ injection, rock degradation is expected. Hydrogen injection in UHS porous reservoirs may trigger the dissolution of carbonates and sulfates, as well as grain crushing and local compaction, possibly altering the reservoir porosity and mechanical and/or flow properties [2]. The response will be time-dependent, with pH equilibration to higher values potentially leading to further compaction and stiffening of the reservoir. However, this effect is likely to stabilize after a few cycles. Consequently, the poroelastic response of the reservoir will heavily depend on the chemical environment in the early stages of operations and become more stable and predictable in later stages.

3.2. Effect on faults

From a geochemical point of view, gas injection may also affect faults, which represent the key factors responsible for fluid migration and containment. Gas injection can affect fault permeability, reactivation potential, and overall stability, which could lead to unintended fluid pathways or seismic activity. Concerning CO₂, during the storage phase over long periods (of the order of thousands of years), fluid-rock interactions can lead to changes in fault rock fabric and mineralogy. This may result in fault frictional properties and cohesion alterations due to dissolution and cementation processes [10]. However, laboratory friction tests comparing fault rocks exposed to CO₂ for several hours to samples taken from natural analogs exposed to CO₂

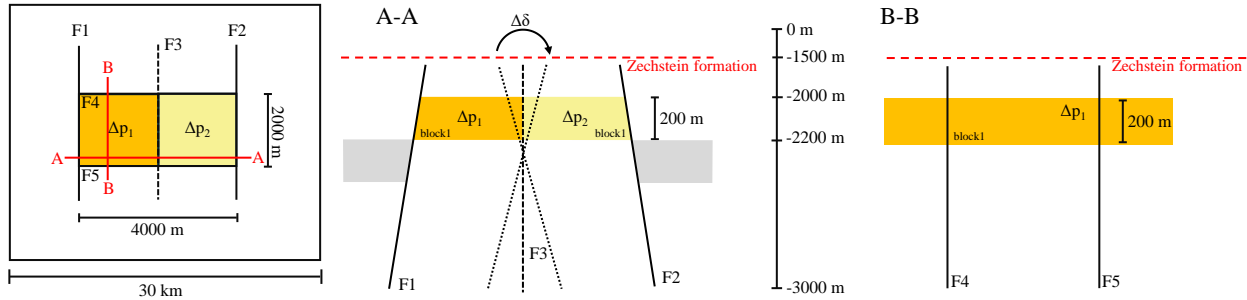


Figure 3: On the left: top view of the conceptual model. On the right: vertical sections of the conceptual model along the trace A-A and B-B.

over millions of years, show limited friction reduction due to CO_2 exposure [47]. Moreover, no specific laboratory studies show how CO_2 -enhanced dissolution and re-precipitation processes may impact on fault cohesion. Based on the literature, the chemical effects on fault mechanical properties after CO_2 injection are considered as negligible.

Finally, there is a lack of documentation on the effect of H_2 and N_2 injection on faults. Experience with underground hydrogen storage in porous geological formations is minimal, with practical applications restricted to the storage of town gas, i.e., a mixture of gases containing 25–60% hydrogen, along with smaller amounts of CH_4 , CO , and CO_2 [24]. Injecting hydrogen into a porous reservoir can change the chemical equilibrium of the formation pore water, leading to fluid-assisted grain-scale processes such as cement dissolution, clay mineral sorption/desorption within grain boundaries, stress corrosion cracking, dissolution-precipitation, and/or intergranular frictional slip [24]. Although these grain-scale mechanisms are well-studied, little is known about the specific effects of hydrogen and nitrogen on their rates.

4. Model set-up

We use the mathematical and numerical framework developed, discussed, and tested in Part I of this work [17]. The modeling approach consists of one-way coupled Finite Element (FE) hydro-poromechanical simulations in fractured geological media. For all the details, the reader is referred to [17].

4.1. Conceptual reference model

The domain geometry conceptually reproduces the compartmentalization commonly observed in the UGS fields of the Rotliegend formation and already sketched in [17]. The reservoir compartments are approximately located at the center of a $30 \times 30 \times 5$ km domain (Figure 3). The reservoir is 200-m thick, 2,000-m deep, and composed by two adjacent 2×2 km blocks. The two reservoir compartments are separated by a fault (F3) and confined by two sets of orthogonal faults (F1-F2 along the y-axis, F4-F5 along the x-axis). Depending on the sealing properties of fault F3, the two compartments can have a partial hydraulic connection. The faults extend from 3,000-m to 1,600-m depth and terminate in the Zechstein salt formation, sealing the reservoir on top. Faults F1 and F2 have a dip angle of $\pm 85^\circ$, while faults F4 and F5 are vertical. The dip angle of fault F3 can vary from $+65^\circ$ to $+90^\circ$ (vertical) and from -90° (vertical) to -65° . Block 2 can be shallower or deeper, with a maximum offset of 200 m, with respect to the Block 1.

The 3D domain is discretized by 8-node hexahedra, with 253,165 nodes and 236,208 elements. A finer discretization is used between 1,800 and 2,200 m depth. Here, the reservoir

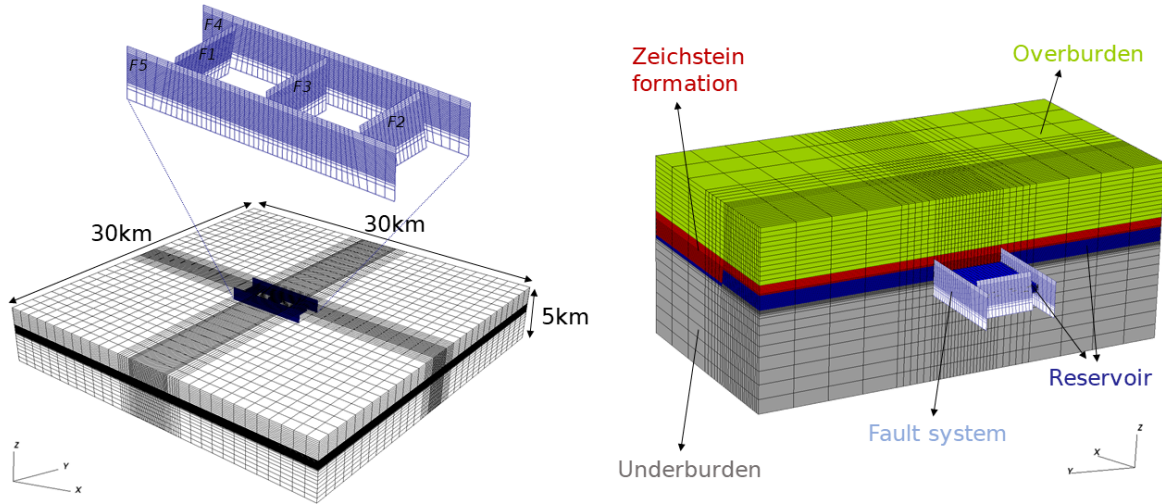


Figure 4: Axonometric view of the 3D computational grid used for the geomechanical simulation and the embedded 2D grid used to represent the fault system.

Layer	Density [kg/m ³]	Young Modulus [GPa]	Poisson ratio [-]
Overburden	2200	10.0	0.25
Zechstein Salt	2100	40.0	0.30
Reservoir (Upper Rotliegend)	2400	11.0	0.15
Underburden	2600	30.0	0.20

Table 1: Formation-dependent geomechanical parameters.

element characteristic size is $100 \times 100 \times 20$ m. The fault system embedded in the 3D grid is discretized by 5,215 zero-thickness contact elements. Standard boundary conditions with zero displacements on the outer and bottom surfaces are prescribed, whereas the top surface, representing the ground, has a stress-free condition. Figure 4 shows a view of the discretized domain with the embedded fault system.

The setting of the reference scenario is established on the basis of the hydro-geomechanical properties of the Rotliegend formation [3, 6, 23, 41, 57] and the frictional properties of faults intercepting the Rotliegend together with immediate overburden and underburden formations [28, 27]. Fault F3 is kept vertical, with no offset between the reservoir blocks. Overburden, caprock, reservoir, and underburden are assumed to behave elastically, with the properties reported in Table 1. Faults are governed by Coulomb’s failure criterion with cohesion $c = 2$ MPa and static friction angle $\varphi_s = 30^\circ$. A linear slip-weakening is also possible with a reduction to the dynamic friction angle φ_d at a sliding amount equal to d_c [17]. As to the undisturbed stress regime, the vertical effective stress, σ_v , is a principal component. The other two horizontal principal components of the effective stress tensor, σ_H and σ_h , are characterized by confinement factors $M_1 = \sigma_h/\sigma_v = 0.74$ and $M_2 = \sigma_H/\sigma_v = 0.83$, with σ_h orthogonal to F1, F2, and σ_H orthogonal to F4 and F5. The value of σ_v is computed from the formation density, assuming a hydrostatic pore pressure distribution.

4.2. Sensitivity analysis

A sensitivity analysis has been developed within the range of some geological and geomechanical quantities to investigate the configurations that are more likely to generate “unexpected” fault reactivations during the injection and storage of different kinds of fluid. The analysis addresses the role of: (i) the geological setting, by varying geometry and properties of faults and reservoir rock, (ii) the poro-elastic stress change with respect to the natural stress

Paper section	Scenario	Parameter/mechanism
5.2	1	reference
5.3.1	2a	Fault F3 with dip angle $\delta = +65^\circ$
	2b	Fault F3 with dip angle $\delta = -65^\circ$
	2c	Block 2 moved down by the offset $o = 100$ m
	2d	Block 2 moved down by the offset $o = 200$ m
5.3.2	3a	Fault cohesion $c = 0.5$ MPa
	3b	Fault static friction angle $\varphi_s = 20^\circ$
	3c	Linear slip-weakening with $\varphi_d = 10^\circ$ and $d_c = 2$ mm
	3d	Linear slip-weakening with $\varphi_d = 20^\circ$ and $d_c = 20$ mm
	4a	Reservoir Young's modulus $E = 8$ GPa
	4b	Reservoir Young's modulus $E = 20$ GPa
5.3.3	5a	UGS uneven ΔP : $\Delta P_1 = -10$ MPa, $\Delta P_2 = 0$ MPa
	5b	UGS uneven ΔP : $\Delta P_1 = -10$ MPa, $\Delta P_2 = -20$ MPa
5.3.4	6a	Principal stress σ_H and σ_h rotated by $\theta = 90^\circ$
	6b	Ratios $M_1 = \sigma_h/\sigma_v = 0.40$ and $M_2 = \sigma_H/\sigma_v = 0.47$

Table 2: Scenarios addressed in Stage 1 of the sensitivity analysis (UGS).

regime, and (iii) the space and time distribution of pore pressure gradients in the reservoir compartments. The analysis has been carried out in two stages:

1. one parameter at a time is modified with respect to the reference scenario with CH₄ storage/production. This enables a thorough analysis of the individual influence of each parameter. The considered variables and scenarios are summarized in Table 2;
2. simultaneous variation of more than one parameter, as identified from Stage 1. Chemical effects were also accounted for by either weakening or hardening the Young modulus by 30% according to the type of injected fluid [4].

Note that the objective of this analysis is to reproduce realistically the actual settings of the Rotliegend formation, rather than to investigate “extreme” conditions.

The main interest of this study is focused on the fault behavior, and in particular the stress conditions yielding a potential sliding. According to the classical Coulomb failure criterion, fault stability is guaranteed if the modulus τ of the shear stress is smaller than its limiting value τ_L :

$$\tau < \tau_L = c + \mu(\sigma_n - P_f), \quad (1)$$

with μ the friction coefficient, i.e., the tangent of the friction angle, σ_n the normal compressive stress, and P_f the fluid pressure in the fault. Wherever $\tau = \tau_L$, sliding is allowed with a potential energy release, while the condition $\tau > \tau_L$ is forbidden. Three parameters are used to evaluate quantitatively the fault state: (i) the criticality index $\chi = \tau/\tau_L$, and, where $\tau = \tau_L$, (ii) the reactivated area t_a , and (iii) the sliding d . Clearly, from Eq. (1) we have $\chi \in [0, 1]$. The closer χ to 1, the more likely is a fault activation. In particular, in the sensitivity scenarios the maximum criticality factor (χ_{\max}), the maximum sliding (d_{\max}), and the fault area (t_{80}) where χ exceeds 0.8 are used to lump the faults' behavior.

5. Modeling Results

5.1. Fluid-dynamic model

The gas flow dynamic during injection and withdrawal is simulated by different codes according to the selected fluid: OPM Flow [53, 44] for CH₄ (UGS), and Eclipse [48] for H₂ (UHS),

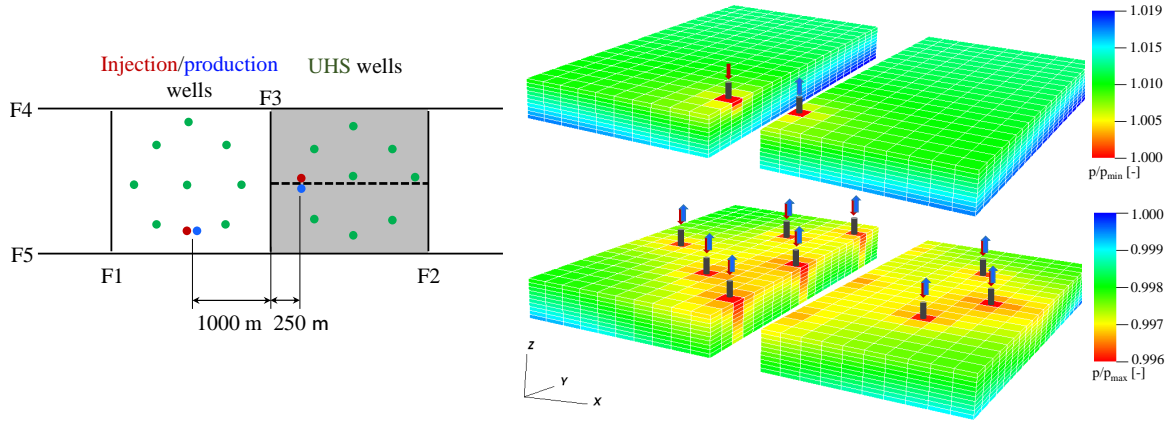


Figure 5: Left: spatial location of the injection and production wells (blue and red for injection/production for CH_4 , red for CO_2 and N_2 injection, and green for UHS cycles). Right: normalized pressure distribution from the flow-dynamic simulation of CH_4 (top) and H_2 (bottom) within the right reservoir block. The grid splits vertically along the dashed line shown on the left panel to provide evidence of the pressure distribution along the vertical direction.

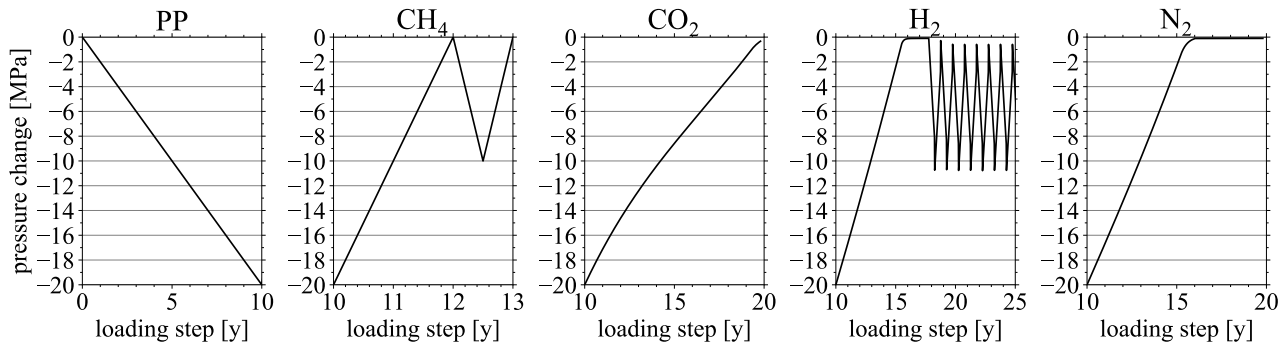


Figure 6: Schematic evolution of pore pressure variation in time for the investigated fluids. The leftmost panel is the common pressure decline during the primary production stage.

CO_2 (CCS), and N_2 . For all simulations, the same well configuration is used. During the PP stage, two wells located next to the reservoir boundary are open in the first layer. Then, these wells are converted to injection purposes. Only for UHS, nine storage wells serve for injection and withdrawal. These wells are rather uniformly distributed throughout the reservoir, as there are no structural or petrophysical characteristics to suggest specific well locations. In Figure 5, the location of the injection and withdrawal wells is shown with respect to the fault system. To avoid interpolation between different computational grids, both OPM and Eclipse finite volume cells coincide with the hexahedral elements of the geomechanical model. Each reservoir block is subdivided into 4,000 regular cells with a $20 \times 20 \times 10$ partitioning. The horizontal and vertical permeability is $k_h = 600$ mD and $k_v = 300$ mD, respectively.

The injection-withdrawal history is depicted in Figure 6. The PP stage is conventionally set to 10 years, with a maximum pore pressure drop of about 20 MPa. The targeted final Recovery Factor, i.e., the ratio between the cumulative produced volume of gas and the gas originally in place, is 90%, in line with theoretical reference behavior for a depletion-driven gas reservoir. Then, for CH_4 the reservoir pressure recovers to the initial value in two years during the CGI phase and a set of UGS cycles, consisting of 6-month withdrawal and 6-month injection each with a 10-MPa pressure, follows. The simulation results show that the pressure change throughout the withdrawal (or injection) phase in a single UGS cycle remains nearly

uniform in space. Hence, employing a uniform pressure change within each block at every loading step could also be justifiable. As to the other fluids, the pressure history is targeted to closely approximate the maximum static pressure drop and recovery in reservoir observed for CH₄, imposing realistic storage constraints. Consequently, the 20-MPa pressure recovery increment during CGI is achieved in a longer period compared to the CH₄ storage scenarios. In addition, no injection/withdrawal cycles are simulated for CO₂ and N₂ storage. The CO₂ storage scenario considers a maximum injection rate of $4 \cdot 10^6$ Sm³/day per well for 13 years before recovering the initial pressure value. Injection of N₂ lasts 6 years with an injection rate of $4 \cdot 10^6$ Sm³/day per well. Concerning H₂, 10 years of injection/withdrawal activity are simulated after a 13-year refilling phase at a maximum rate of $4 \cdot 10^6$ Sm³/day per well. Each UHS cycle consists of a 6-month withdrawal and a 6-month injection period, with a maximum pressure variation of 10 MPa. In all simulations, a 1-year loading step (l.s.) is used during PP and CGI/refilling, while during UGS and UHS the loading step is equal to 15 days.

It is important to recall that in the Netherlands the fluid pressure is not allowed to exceed the initial value P_i .

Pore pressure propagation within the fault zone varies according to the distribution of pressure changes across different reservoir compartments. When differing pressure changes occur on opposite sides of the fault, the resulting pore pressure change within the fault, denoted as ΔP_f , correspond to the average of the pressure changes from both sides. The fluid pressure in the fault, P_f , generates forces that oppose to the action of the pressure variation on σ_n .

5.2. Mechanisms of fault re-activation: reference case (Scenario #1)

The basic fault reactivation mechanisms are studied in scenario #1, which serves as the reference scenario for UGS activity with CH₄. A few preliminary outcomes can already be found in [51, 52, 17]. For the sake of completeness, they are briefly summarized here as well.

Figure 7 shows the behavior of the maximum χ value, χ_{max} , experienced on faults F1 through F5 for 13 years, i.e., PP, CGI and the first UGS cycle. Faults F1 and F2 can reach a critical condition at the end of the PP stage. During CGI and UGS, the fault activation risk reduces, with χ_{max} decreasing to about 0.80. During CGI, χ_{max} initially decreases, i.e., the fault returns more stable, but then increases again, with the shear stress acting in the opposite direction with respect to that experienced during PP. The time behavior of the maximum sliding d_{max} computed for each fault is also shown in Figure 7. These two quantities, i.e., χ_{max} and d_{max} , are closely related to each other, since a single element can slide only when $\chi = 1$. Notice that, to obtain information on the criticality state of the entire fracture at a given depth, the provided χ_{max} represents the value averaged on the stripe of fault elements located at the same depth. For this reason, it is possible to detect sliding conditions even when the χ value reported on the top frame of Figure 7 is smaller than 1. Fault F1, F2, F4, and F5 can start sliding between year 4 and 6. The maximum sliding can be of about 1.4 cm. Fault F3 remains unaffected throughout the loading and injection steps due to the model symmetry. The most critical condition develops along the top and bottom of the reservoir. Figure 8 shows the behavior of χ with respect to depth on all the fracture surfaces at loading step 10.

The mechanisms leading to the possible fault reactivation can be better understood in terms of shear stress τ (bottom frame of Figure 7), particularly at loading steps 0, 10 (end of PP), 11, 12 (end of CGI), 12.5 (end of UGS withdrawal), and 13 (end of UGS injection). The largest values are computed at the end of primary production, with opposing shear stress orientations at top and bottom of the reservoir. During PP, the direction of the shear stress is always oriented toward the reservoir mid-plane. At loading step 4 and 5 sliding starts (middle of Figure 7) at reservoir top and bottom. The elements surrounding the activated fault portions increase

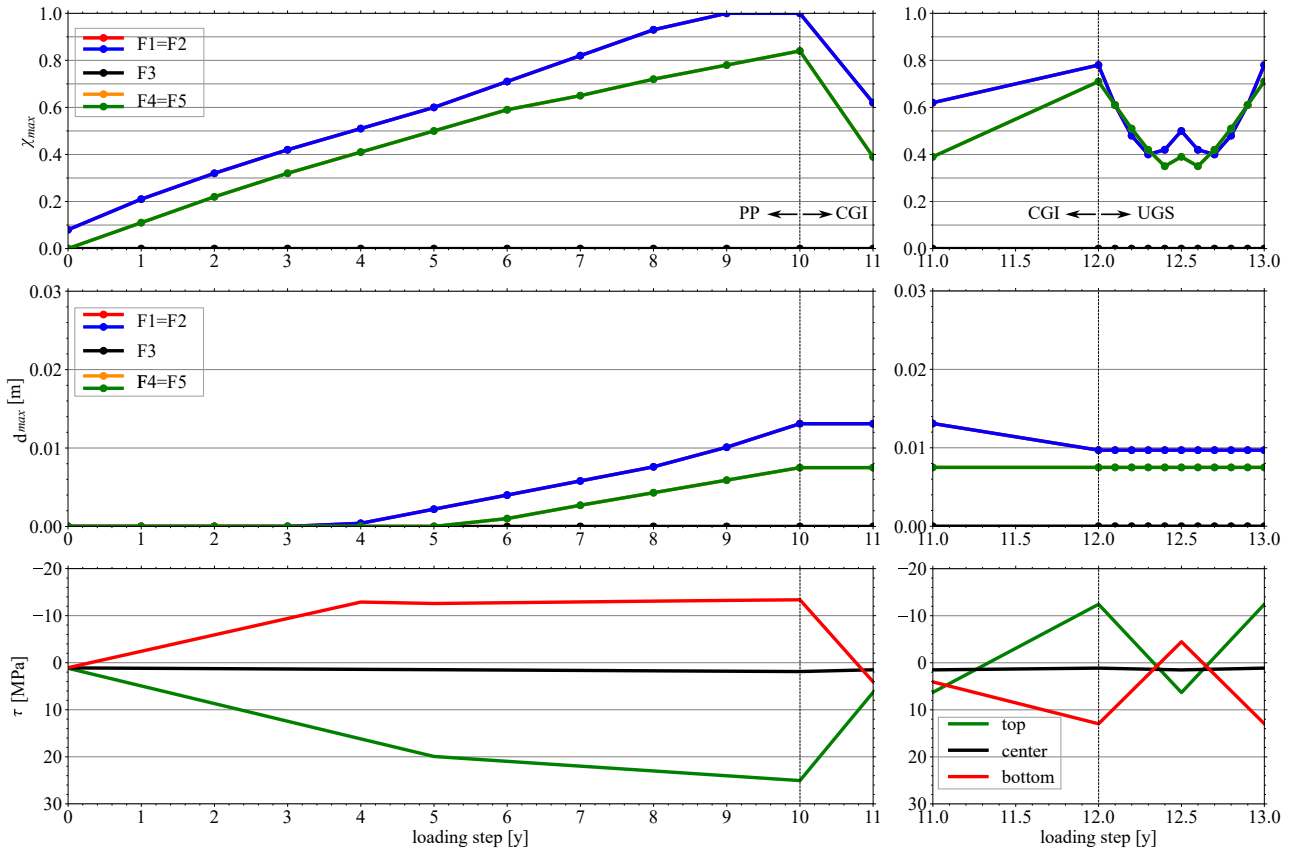


Figure 7: Scenario #1: χ_{max} (top), d_{max} (middle), and τ (bottom) over time for all faults. Positive values for the shear stress means that it is upward oriented.

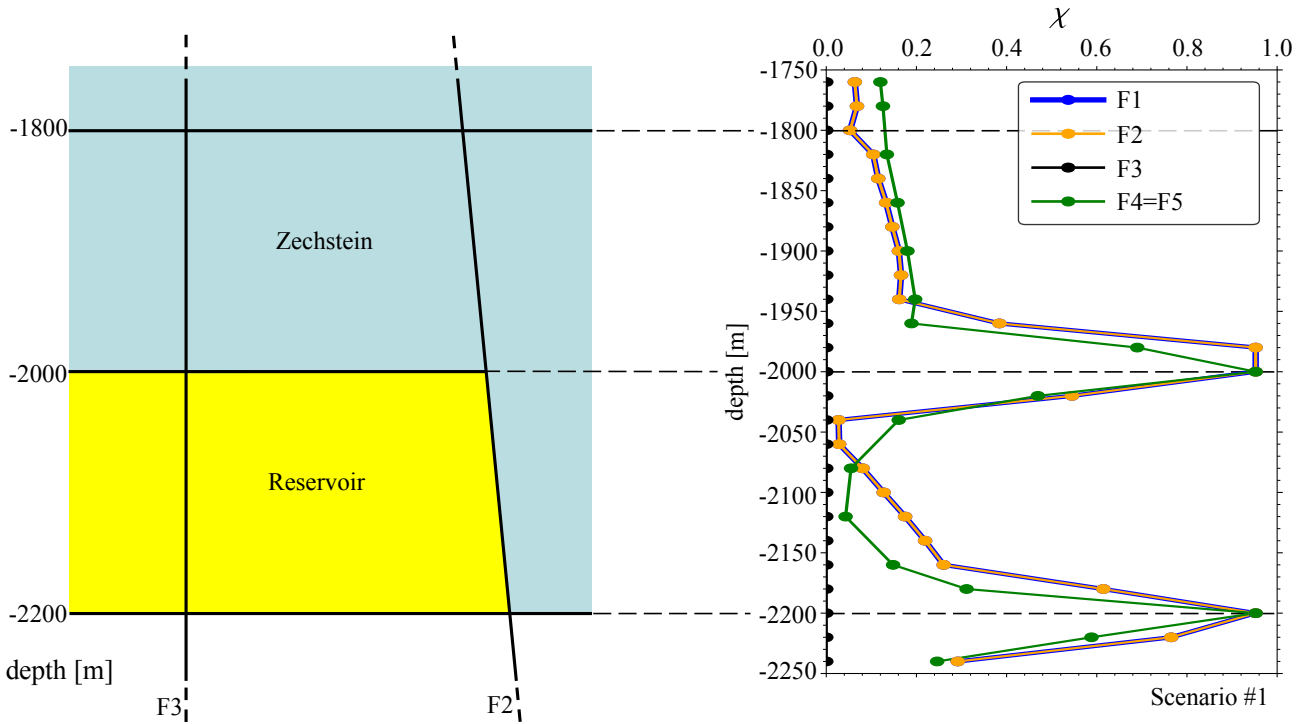


Figure 8: Scenario #1: χ in depth at the end of PP.

their shear stress to accommodate the excess to the Coulomb frictional limit not supported by the activated (sliding) elements. At loading step 11, half of the pore pressure change has been recovered. As the reservoir expands due to pressure recovery, the shear stress changes direction and annihilates approximately the shear stress acting on the previously sliding elements. The reservoir continues to recover pressure and re-expand until loading step 12. During the second half of cushion gas injection, the shear stress increases again, with a direction opposite to that experienced during primary production. The expansion during CGI can generate again a critical condition on the fault, with a possible localized reactivation at the reservoir top due to the stress redistribution following the sliding. During UGS, at the end of the production phase (loading step 12.5), the shear stress almost equals the condition at loading step 11. Correspondingly, the shear stress at loading step 13 equals the stress state at loading step 12. Indeed, during UGS, sliding does not occur, and the porous medium behaves according to a linear elastic constitutive law. This complex behavior is also confirmed by the analysis of the stress path experienced by some representative elements, as reported in [17].

5.3. Sensitivity analysis: Stage 1

Starting from the reference configuration of scenario #1, we explore how variations in individual geometric or mechanical parameters can affect the outcomes. We conducted an extensive investigation, of which we report here the most significant results, referring to the scenarios summarized in Table 2 for the UGS analysis with CH₄. Other simulations were carried out, but are not discussed here for the sake of brevity. The outcomes are cross-compared to identify the settings that make the subsurface system more prone to fault reactivation. For the analysis, we use the parameter t_{80} , i.e., the areal extent where $\chi \geq 0.80$. Such areal extent is scaled by 2,000 m, which is the characteristic size of each reservoir block, so that t_{80} has the size of a length. For the sake of simplicity, we focus on faults F2 and F3, unless differently specified.

5.3.1. Reservoir and fault geometry

The impact of fault geometry is investigated by varying the dip angle of the central fault F3 (#2a - #2b) and increasing the offset between reservoir compartments of half (#2c) and entire (#2d) reservoir thickness. Figure 9 shows χ_{max} over time for the reference and the #2a - #2d scenarios. Interestingly, while the geometry variation has no effect on fault F1, a large offset between the reservoir compartments (scenario #2d) enhances the potential for instability in faults F4 and F5. The instability of fault F2 is slightly increased by a variation of the fault geometry, however this becomes significant only when a large offset between compartments is introduced (#2d).

In the latter configuration, unlike the reference scenario, fault F3 is significantly affected by the asymmetry of the system. Indeed, it becomes active and experiences the highest stress levels at the top and bottom of each compartment. Differently from the reference scenario, χ_{max} on fault F3 can now reach the limiting value. Furthermore, χ_{max} achieves the alert threshold of 0.8 also during CGI and UGS, suggesting that UGS operations in this condition might be critical. Consistently, fault F3 exhibits the highest sliding value $d_{max} = 7.4$ cm at the end of the PP phase (Figure 10). Some instability can also occur at the end of the UGS cycle. The other faults can activate around the loading step 4, again at the reservoir top first, and at the reservoir bottom later. Figure 11 shows the active elements within the embedded fault discretization at loading step 6, 10 (end of PP), and 12.5 (middle of a UGS cycle).

5.3.2. Geo-mechanical parameters of faults and reservoir

The investigation continues further into the effect of Coulomb rupture criterion and reservoir stiffness. Concerning the Coulomb parameters, the variation of both the cohesion (#3a) and

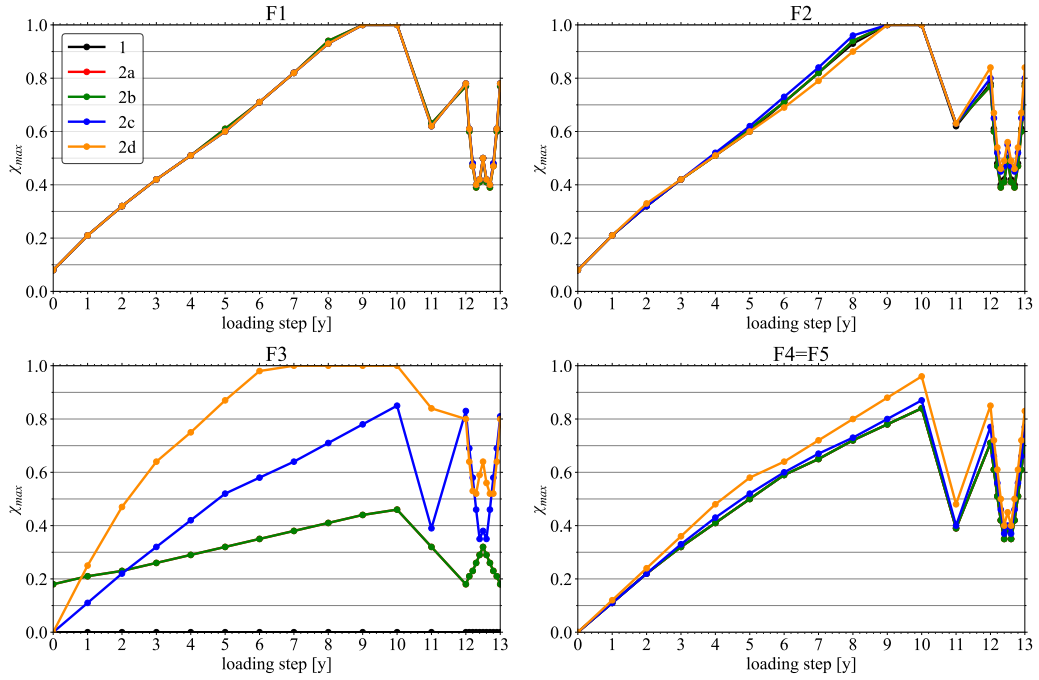


Figure 9: Scenarios #2: χ_{max} over time for each fault. Note that F4 and F5 exhibit an identical behavior, due to symmetric conditions.

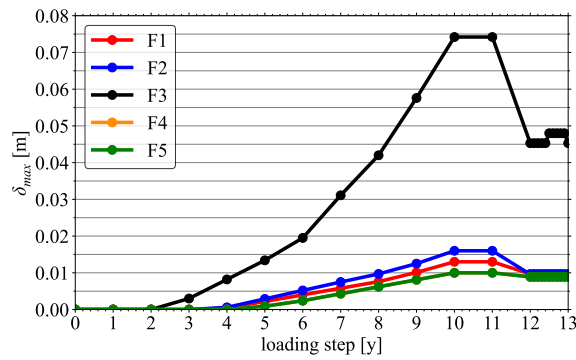


Figure 10: Scenario #2d: maximum sliding d_{max} .

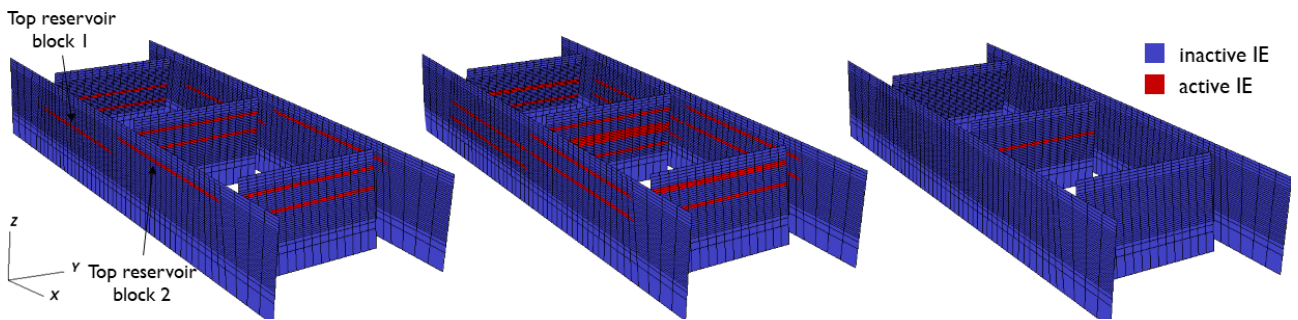


Figure 11: Scenario #2d: active interface elements (IE) on the fault system at loading step 6 (left), loading step 10 (center), and loading step 12.5 (right). Only the elements at the reservoir top, and then bottom, are activated.

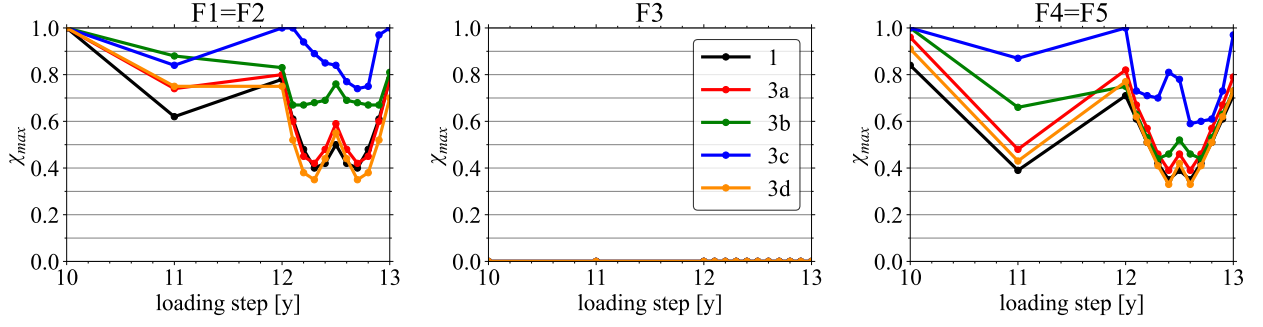


Figure 12: Scenarios #3: χ_{max} over time for the CGI and UGS phases.

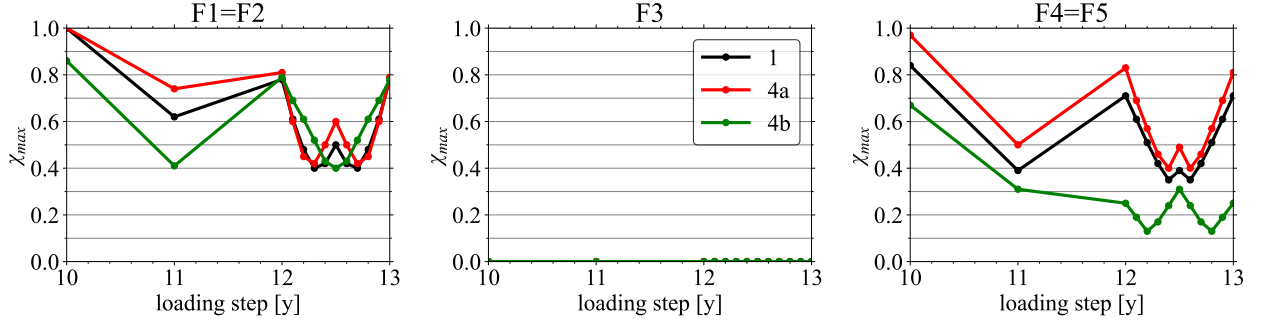


Figure 13: Scenarios #4: χ_{max} over time for the CGI and UGS phases.

friction angle (#3b) exerts a significant influence on fault stability, mainly during the PP and CGI phases. A reduced friction angle, in particular, weakens the resistance to fault reactivation.

The mechanism of fault weakening is investigated by using slip-weakening constitutive law for the fracture behavior [17]:

$$\varphi = \begin{cases} \varphi_s + \frac{\varphi_d - \varphi_s}{d_c} d & \text{for } d < d_c \\ \varphi_d & \text{for } d \geq d_c \end{cases} \quad (2)$$

The two parameters defining the new constitutive law are φ_d and d_c , i.e., the dynamic friction angle and the slip weakening distance, respectively. Slip weakening occurs after sliding begins by reducing the value of the friction angle. The most critical results in terms of fault stability are obtained for scenario #3c, characterized by a reduction of the friction angle from $\varphi_s = 30^\circ$ to $\varphi_d = 10^\circ$ in a slip distance of $d_c = 2$ mm. The behavior of χ_{max} for scenarios #3 during the CGI and UGS stages is reported in Figure 12, showing that slip-weakening may cause a reactivation also at loading steps 11 and 13, but not at loading step 12.5, i.e., in the middle of a UGS cycle.

The relationship between reservoir stiffness and fault behavior has been further investigated in Scenarios #4. A significant contrast between the reservoir and the surrounding caprock, sideburden, and underburden stiffness may play an important role to induce a critical stress state on faults. In scenario #4a, the reservoir is softer than the surroundings, and this generally increases the likelihood of a fault reactivation (see Figure 13). Conversely, in scenario #4b, the fault reactivation likelihood is notably reduced. During the UGS stage, χ_{max} remains below 0.7, regardless of the reservoir stiffness value (see Figure 13).

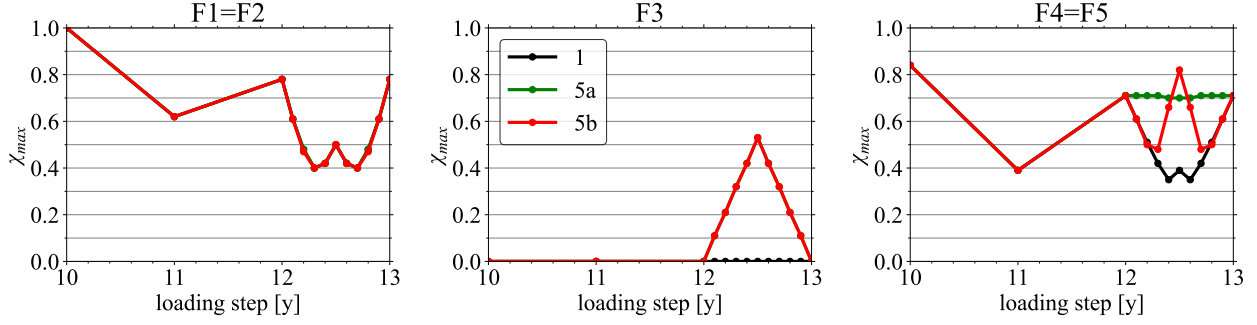


Figure 14: Scenarios #5: χ_{max} over time for the CGI and UGS phases.

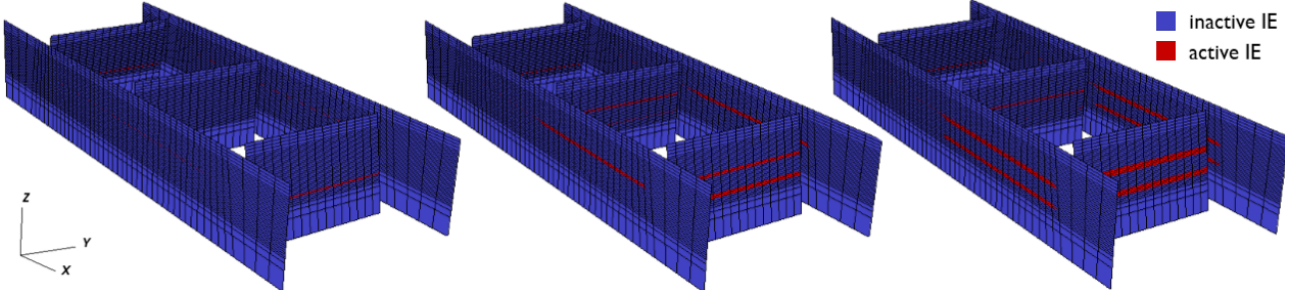


Figure 15: Active interface elements (IE) on the fault system at loading step 12.5 for scenario #1 (left), #5a (center) and #5b (right).

5.3.3. Uneven pore pressure excursion in the reservoir compartments

The effect of a different pore pressure change in the two reservoir compartments is investigated in Scenarios #5 (Table 2). During UGS, fault F3 and, secondarily, faults F4 and F5, may exhibit larger χ values at loading step 12.5 (Figure 14). When $\Delta P_2 = 0$ MPa, faults F4 and F5 keeps the same critical degree experienced at the end of CGI over the UGS phase. Conversely, with $\Delta P_2 = -20$ MPa the most critical condition is achieved in the middle of the UGS cycle, where χ_{max} is larger than the threshold value 0.80. Figure 15 shows the distribution of the potentially active elements ($\chi \geq 0.80$) in Scenarios #5, again within the embedded fault discretization at loading step 12.5.

For scenario #5b, Figure 16 shows the time behavior of χ_{max} and the shear stress modulus τ at the reservoir bottom on fault F4. The shear stress increases during the PP stage, reaching the limit shear stress τ_L at loading step 5. Then, τ equates τ_L at the end of CGI and at the end of UGS production and injection cycle. On fault F2, χ_{max} approaches 1 at the end of the UGS injection phase too, but remains well below the criticality value at the end of CGI phase.

5.3.4. Initial stress regime

The orientation on the principal components of the stress tensor in undisturbed conditions is another key factor for predicting the fault stability during the reservoir management. This is analyzed in Scenarios #6. The modeling outcome revealed that a rotation of the maximum horizontal stress by 90° (scenario #6a) does not provide a significant variation with respect to the reference case. By distinction, an initial stress regime close to normally consolidated conditions (scenario #6b) significantly increases the fault reactivation likelihood, as it can be appreciated from the t_{80} values in Figure 17. Although the occurrence of such a scenario is unlikely, it is important to consider its implications. With the undisturbed stress regime of scenario #5b, the limit $\chi_{max} = 1$ is reached at an earlier point of the PP stage on faults F1 and F2 (loading step 6) and F4 and F5 (loading step 8), resulting in a larger fault area that is prone

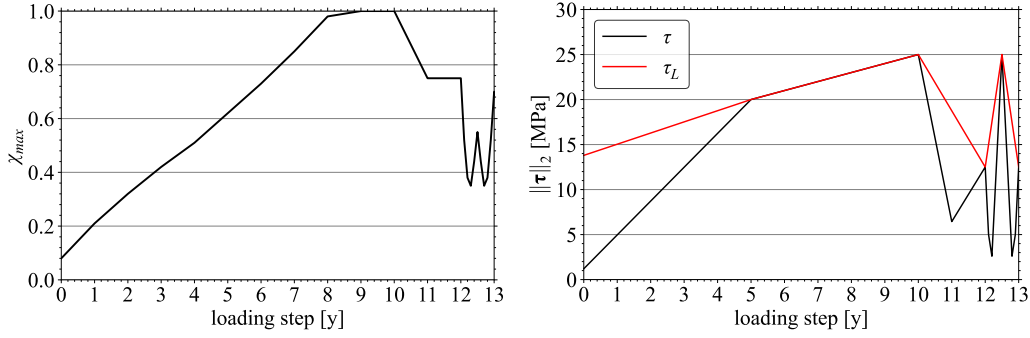


Figure 16: Scenario #5b: χ_{max} over time on fault F1 (left), τ and τ_L in time on fault F4 (right).

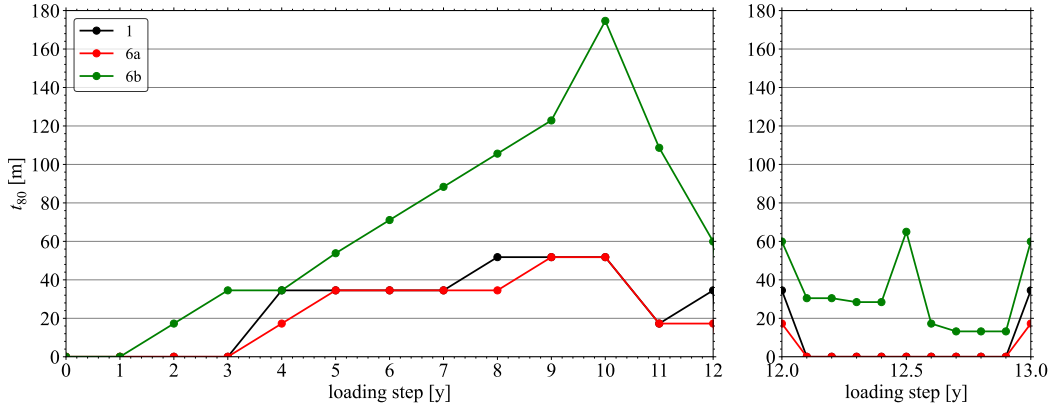


Figure 17: Scenarios #6: t_{80} over time on fault F2. A zoom for the UGS stage is provided on the right panel of the figure.

to a potential reactivation (Figure 17). The earlier activation during PP causes a reactivation of faults F1 and F2 at the end of the CGI and UGS stages as well.

5.3.5. Ranking factors favoring fault reactivation

The objective of this section is to define criteria to rank the potential of inducing “unexpected” seismic events for the different investigated scenarios. The analysis focuses on fault F3, which is the most stressed in the realistic condition of a compartment offset, and fault F2, representing the behavior at the reservoir boundaries. The results are presented in Table 3. The ranking process takes into account the following quantities, from the most to the least important one:

1. χ_{max} during UGS stage;
2. the maximum value of average sliding d_{avg} ;
3. the loading step of first activation.

As expected, fault activation during CGI and UGS cycles exhibits distinct critical factors for boundary and central faults. For fault F2, stability is primarily influenced by the initial stress regime of the system, geomechanical properties, like reservoir stiffness, and fault characteristics, such as cohesion, static friction angle, and the presence of slip weakening. In contrast, for fault F3, geometric parameters play a major role. The stability of fault F3 is strongly influenced by a compartment offset, non-vertical fault planes, and differential pressure changes in the two compartments.

Scenario	Fault F2				Scenario	Fault F3			
	χ_{max} UGS	Max d_{avg} [m]	Act. year	χ_{max} PP		χ_{max} UGS	Max d_{avg} [m]	Act. year	χ_{max} PP
3c	1.00	0.026	7	1.00	2d	0.84	0.033	7	1.00
5b	0.97	0.010	9	1.00	2c	0.81	0.007	-	0.85
6b	0.96	0.018	6	1.00	5a	0.53	0.000	-	0.53
2d	0.84	0.008	9	1.00	5b	0.53	0.000	-	0.53
3b	0.81	0.010	7	1.00	2a/b	0.32	0.000	-	0.46
2c	0.80	0.007	9	1.00	1	0.00	0.000	-	0.00
4a	0.79	0.010	8	1.00	6a	0.00	0.000	-	0.00
3a	0.78	0.008	8	1.00	6b	0.00	0.000	-	0.00
1	0.78	0.007	8	1.00	3a	0.00	0.000	-	0.00
5a	0.78	0.007	9	1.00	3b	0.00	0.000	-	0.00
2a/b	0.77	0.007	8	1.00	3c	0.00	0.000	-	0.00
6a	0.74	0.007	10	1.00	3d	0.00	0.000	-	0.00
3d	0.70	0.009	8	1.00	4a	0.00	0.000	-	0.00
4b	0.78	0.005	-	0.78	4b	0.00	0.000	-	0.00

Table 3: Ranking of the simulated scenarios according to the largest χ_{max} in the UGS stage, the largest sliding, and the earliest first activation step.

Combination	Parameter/mechanism
C1	$c = 0$ MPa, $\delta = +65^\circ$, $o = 100$ m
C2	$\varphi_s = 20^\circ$, $\delta = +65^\circ$, $o = 100$ m
W	E decreased by 30% during injection
H	E increased by 30% during injection

Table 4: Combination of settings addressed in Stage 2 of the sensitivity analysis for the fluids under consideration.

5.4. Sensitivity analysis: Stage 2

In the second stage of the sensitivity analysis, we combine the most influential factors for yielding a potential fault reactivation, as identified in Stage 1, and test the new scenarios for the storage of different gases, namely CH₄, CO₂, H₂, and N₂. The scenarios discussed here are summarized in Table 4. We remember that the primary objective of this analysis is to explain realistic configurations likely to be encountered in the Rotliegend formation, rather than to explore “extreme” conditions. Therefore, taking into account the most influential factors from Stage 1, we chose to focus on the combinations presented in Table 4. They combine a compartment offset, non-vertical fault planes, and variations in the fault characteristics, i.e., cohesion (C1) and static friction angle (C2). Two dedicated combinations analyze the effect of different geomechanical properties, i.e., decreasing (W) and increasing (H) of the reservoir stiffness, most likely associated to chemo-mechanical effects.

The potential risk of fault reactivation is evaluated for each scenario by the parameter t_{80} , whose behavior in time is shown in Figure 18. Regardless of the fluid, Figure 18 shows that the combination C2 provides the conditions yielding the larger t_{80} values. This scenario is characterized by a compartment offset and a reduced friction angle. Conditions close to reactivation occur during both CGI and UGS/UHS, or long-term storage, stages. Notice that t_{80} after the end of PP is larger if the faults already experienced a significant reactivation (i.e., with a large t_{80}) during PP. As compared to other critical combined configurations, such as C1, scenario C2 is more critical primarily because of the reduction of the friction angle.

Due to its significance, the outcomes of the critical combination C2 have been separately

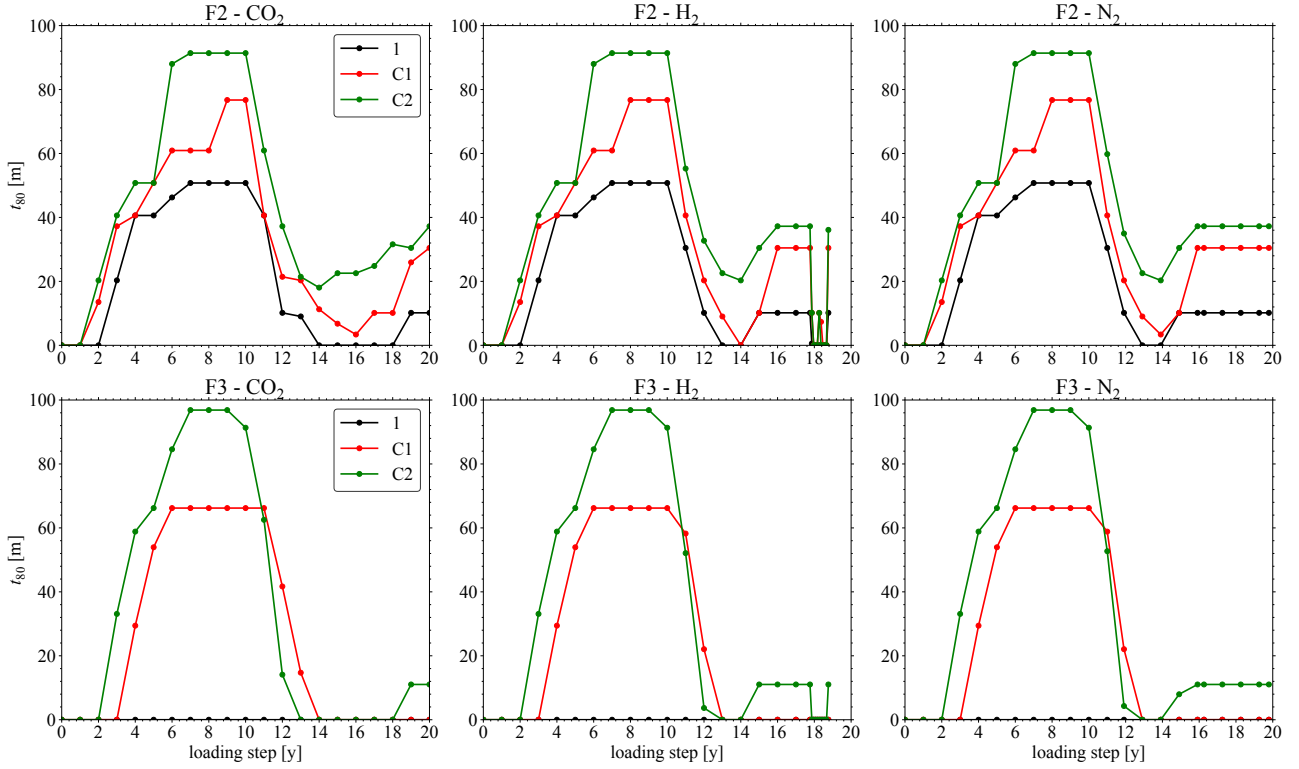


Figure 18: Sensitivity analysis, Stage 2: t_{80} over time for fault F2 and F3 and the different fluids under investigation.

described for CH_4 and the other gases. This distinction is made based on the differences in pressure history (see Figure 6).

5.4.1. UGS critical scenario

The combination of factors in configuration C2 causes a potential reactivation, mainly during primary production. The condition is particularly critical for faults F2 and F3 during the UGS phase, with both faults reaching a critical condition not only at the end of the UGS storage phase but also during withdrawal. Figure 19, which shows χ_{max} in time for scenario C2 as compared to the reference case (scenario #1), highlights that critical conditions for fault reactivation develop earlier during PP. χ_{max} is also greater than, or close to, 0.8 during CGI and UGS. Because of the loss of symmetry, F2 is more stressed than F1 and χ_{max} achieves values larger than 0.8 on fault F3 as well. Figure 20 provides a 3D view of χ distribution in space at a few significant loading steps.

The behavior of d_{max} for all the faults is shown in Figure 21. During the CGI phase, all the faults slide, primarily during the period between loading step 11 and 12, in the opposite direction to what occurred during primary production. Additionally, faults F1, F2, and F3 slightly slide again at the end of the UGS injection phase.

5.4.2. CO_2 , H_2 , N_2 storage dynamics and fault activation

The goal of this section is to compare how the temporary or permanent storage of different gases may influence the fault stability, as measured by χ_{max} in the critical scenario C2. Since the pore pressure variation during PP is the same for each fluid, χ has the same behavior until loading step 10. After that, the impact on fault stability must be considered based on whether temporary or permanent storage scenarios occur.

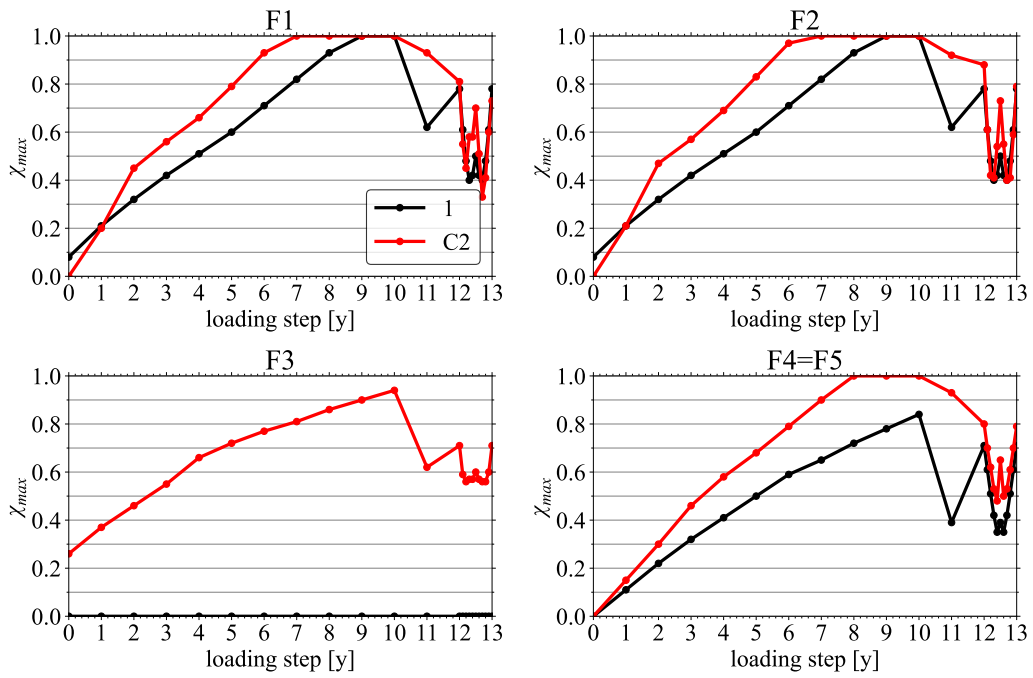


Figure 19: Scenario C2, UGS: χ_{max} over time for all faults compared to the reference case (scenario #1).

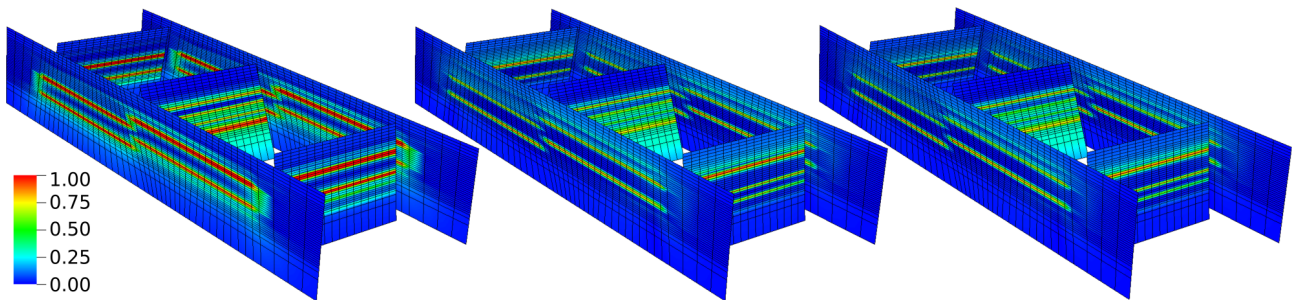


Figure 20: Scenario C2: χ distribution in space on the fault system at the end of PP (left), CGI (middle) and UGS (right).

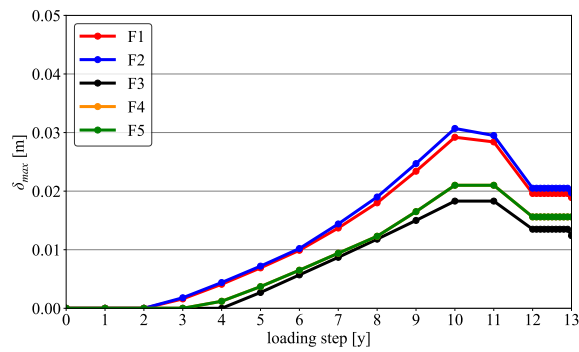


Figure 21: Scenario C2, UGS: maximum sliding d_{max} over time for all the faults.

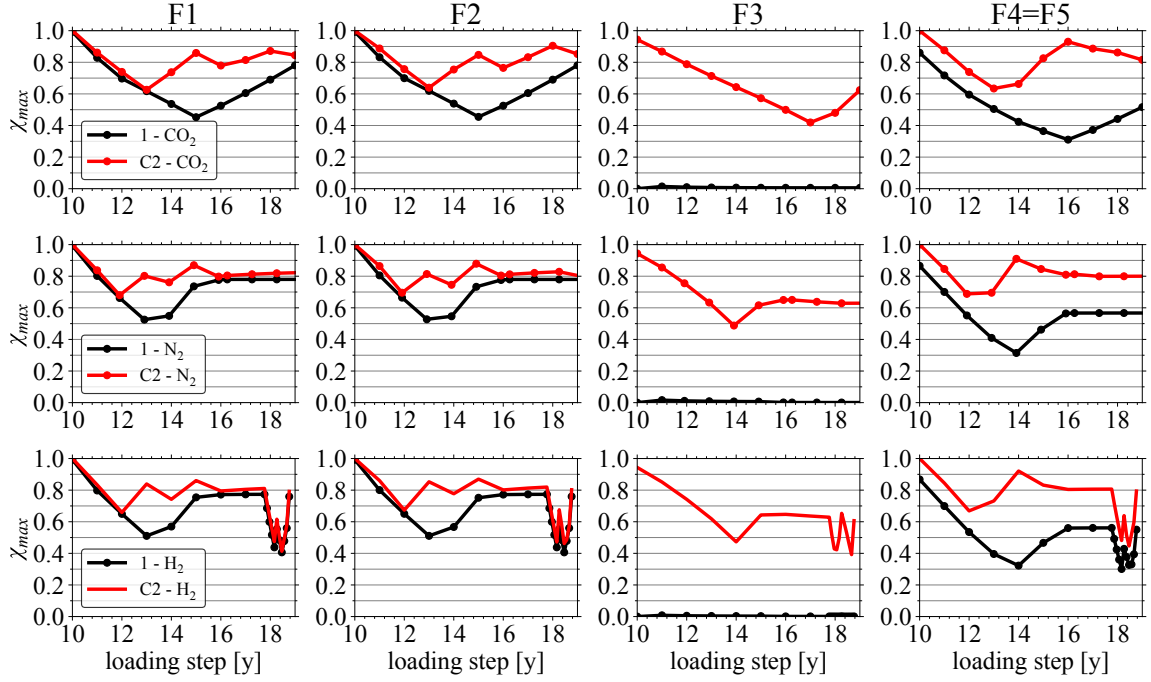


Figure 22: Scenario C2: χ_{max} over time for CO₂, N₂ and H₂ after the end of PP.

For the permanent storage scenarios, i.e., CO₂ and N₂, at the beginning of the storage χ_{max} decreases due to the unloading of the shear stress caused by reservoir expansion. However, as the storage continues, the shear stress is loaded with the opposite sign, reaching a relative maximum at the end of the injection stage. This point corresponds to the full pore pressure recovery (Figure 22). As far as it concerns the injection/withdrawal cycles for H₂, χ_{max} on F1, F2 and F4-F5 reaches its maximum at the end of the injection stage, corresponding to the highest value of pressure in the reservoir. For F3, χ_{max} exhibits an additional peak at the end of the UHS withdrawal stage.

5.4.3. Geochemical effects on fault stability

Geochemical effects are also considered. Based on the literature review summarized in Section 3, we have incorporated the possibility to account for geochemical influences by introducing a hardening/weakening behavior of reservoir rocks. Specifically, during injection the Young modulus is increased or decreased by 30%, depending on the fluid involved. For CO₂, both weakening and hardening scenarios have been observed, depending on the actual rock mineralogical composition. Conversely, H₂ might induce a weakening effect, while N₂ shows a relatively neutral geochemical impact on the reservoir rock.

Figure 23 shows the behavior of χ_{max} for the weakening/hardening scenarios (W/H). Fault F3 remains stable throughout the simulation because of symmetry. During CO₂ injection, with a hardening behavior, χ_{max} first decreases and then increases with respect to the reference case. The opposite occurs for the weakening scenario. Similar considerations hold for H₂ in the weakening scenario, with an even smaller difference with respect to the reference case. Based on these results, we can preliminarily conclude that geochemical effects on the reservoir rock have a minor impact on fault stability.

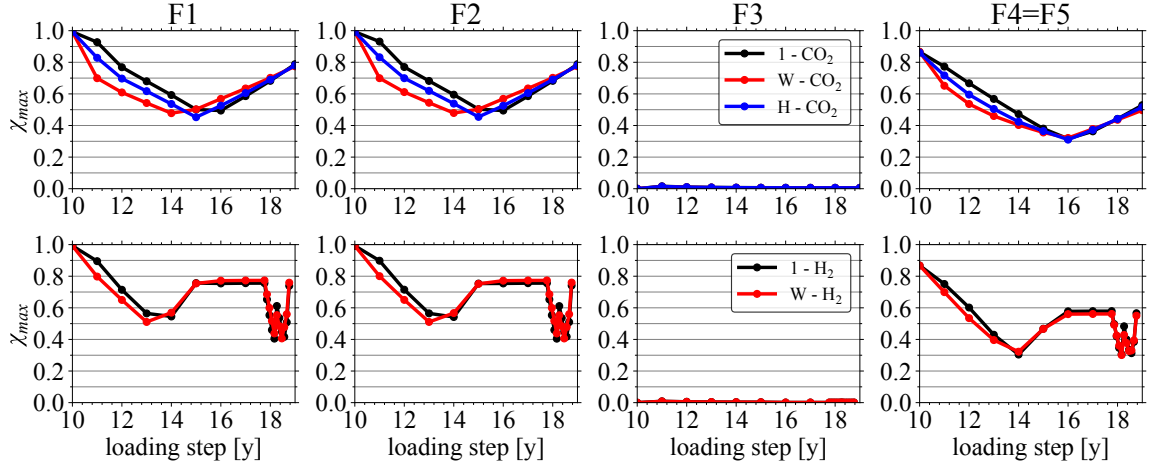


Figure 23: Scenarios W and H: χ_{max} over time for CO₂ (upper) and H₂ (lower).

6. Discussion

6.1. Comparison with previous studies

A few papers addressing the topics of our work have recently been published. Works [62] and [23] are of particular interest because they focus on Rotliegend reservoirs in the Netherlands and northern Germany, providing insights into fault reactivation and fault rupture during primary production. Although the authors: i) do not consider induced seismicity during UGS stages, ii) use a simplified 2D setting, and iii) employ a different modeling approach concerning fault activation, these studies carry out a parametric analysis on the same geometric/geomechanical features investigated in this paper.

The findings of our work mostly align with the outcomes by [62] regarding fault failure mechanisms and slip initiation. Our study confirms that fault slip initiates at the top of the reservoir rocks where the initial *shear capacity utilization* SCU [62], corresponding to our safety factor χ , reaches the maximum values. Both studies agree that faults without offset experience reactivation at later stages of depletion, and fault rupture does not extend upwards into the caprock. Scenarios #2c, #2d, and C2, for example, confirm that in the case of a compartment offset, an earlier fault activation is favored and remains bounded within the reservoir depth range. Regarding the influence of the contrast in elastic properties distribution, our study agrees with [62] only partially. They observed a secondary peak in shear stress at the bottom of the footwall reservoir block and a localized decrease in shear stresses and SCU at the bottom of the hanging wall reservoir block. Qualitatively, the results presented above (see, for example, Figure 22) agree. However, it must be considered that [62] assigned a uniform density and elastic properties to all rocks while our study, in particular scenarios #4a and #4b, demonstrates that the contrast in elastic properties may significantly impact on stress concentration and, therefore, fault failure (Figure 13).

Comparing our results with the findings presented by [23] regarding factors influencing fault reactivation and criticality, we agree that the initial stress regime (scenarios #6a and #6b, Figure 17) plays significant roles in fault behavior. Obviously, this relation is a well known in the literature [16, 40, 61]. Indeed, fault criticality largely increases as the horizontal components of the natural stress regime decrease relative to the vertical stress. Furthermore, our outcomes confirm that the stiffness contrast between the reservoir and surrounding rocks (scenarios #4a and #4b) governs the stress redistribution and the degree of stress rotation during the reservoir development, impacting fault reactivation. According to [23] the depletion of thicker reservoir

horizons results in a stronger fault-loading compared to the depletion of thinner reservoir horizons, as a thick reservoir undergoes a relatively larger strain for a same change of pore fluid pressure. Although our sensitivity analysis did not directly consider reservoir thickness as a parameter, we observed consistent outcomes when a larger strain is attributed to a larger pressure decrease (scenario #5b, Figure 16).

However, there are a few aspects where our project disagrees with findings from [23]. While they suggested that the fault throw should be half of the reservoir thickness to obtain the maximum shear stress ratio values, we found that the most critical condition occurred when the fault offset is equal to the entire reservoir thickness. This discrepancy can be attributed to the different modeling setup, including the horizontal-to-vertical ratio of the natural stress components and the reservoir depth. These disparities emphasize the importance of the modeling approach and setup parameters, highlighting the need for further research to fully understand fault behavior in different geological contexts.

6.2. Definition of safe operational bandwidths

After the end of primary production, when the natural fluid pressure P_i is reduced to $P_{min,PP}$, the reservoir experiences a relatively fast pressure recovery to $P_{max,CGI/CCS}$ during cushion gas injection or gas storage (CO_2 or N_2). Afterward, UGS or UHS are characterized by a cyclic pressure fluctuation between $P_{min,UGS/UHG}$ and $P_{max,UGS/UHS}$ at the end of the production and injection phases, respectively. In the usual practice and in alignment with the legislation of some countries, e.g., the Netherlands, $P_{max,CGI/CCS} \simeq P_{max,UGS/UHS} \simeq P_i$ and $P_{min,UGS/UHS} \geq P_{min,PP}$ (Figure 24-left). In this framework, guidelines for the definition of “safe operation bandwidths” in gas storage, i.e., operations with a reduced risk of fault reactivation, must identify proper values for the aforementioned pressure bounds. Nevertheless, it has to be recalled that a fault reactivation could always occur aseismically [8].

The interpretation of the modeling results allows outlining some key guidelines. They are necessarily qualitative because of the theoretical/general framework of the modeling application and the quasi-static nature of the implemented model, which properly simulates the possible inception of fault slip but not the seismic evolution. The numerous scenarios investigated within the study have clearly revealed that fault failure is more likely to happen during CGI/CCS and UGS/UHS in depleted reservoirs when:

1. fault reactivation is occurred during PP. We refer to the pressure of seismic occurrence as $P_{seis,PP}$. As an example, in scenario #4b faults are not active during PP and remain far from critical conditions during CGI and UGS as well (Figure 13 and Table 3);
2. the reservoir pressure approaches $P_{max,CGI/ST}$, $P_{max,UGS/UHS}$, or $P_{min,UGS/UHS}$ (e.g., Figures 19 and 22).

The resulting guidelines, which link $P_{max,CGI/CCS}$, $P_{max,UGS/UHS}$, and $P_{min,UGS/UHS}$ to $P_{min,PP}$ and $P_{seis,PP}$, can be summarized as follows. The outcome of scenario C2 is particularly illustrative in this regard (Figures 19 and 22).

- If a fault reactivation occurs during PP, the pressure change ΔP spanned during CGI/CCS and UGS/UHS phases should be kept smaller than $|P_i - P_{min,PP}|$. Indeed, a number of investigated scenarios (see, for example, the outcomes of scenarios #2, Figure 9) reveals that fault activation during primary production leads to a stress redistribution and a new deformed “balanced” configuration that is newly loaded, in the opposite direction, when the pressure variation changes its sign. A reasonable rule is to keep ΔP smaller than maximum between $|P_{seis,PP} - P_{min,PP}|$ (range highlighted with a in the middle panel of Figure 24) and $|P_i - P_{seis,PP}|$ (range highlighted with b in the right panel of Figure 24),

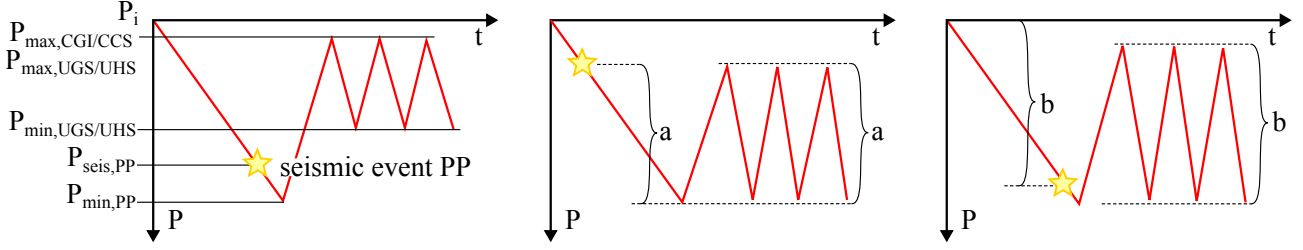


Figure 24: Left: pressure values to be accounted for in the definition of operational safety guidelines. Middle and right: safe pressure variation during CGI, CCS, and UGS/UHS phases in the case of a seismic event occurring during PP at pressure close to P_i and $P_{min,PP}$, respectively.

i.e., the maximum pressure difference experienced by the reservoir during PP without the occurrence of a seismic event. The classification into these two classes is determined by the value of $P_{seis,PP}$ in relation to P_i and $P_{min,PP}$, as illustrated in Figure 24, particularly in the middle and right panels.

- In the former case (middle panel of Figure 24), $P_{max,CGI/CCS}$ and $P_{max,UGS/UHS}$ should be kept below P_i . A reasonable rule of thumb could be to keep $P_{max,CGI/CCS}$ and $P_{max,UGS/UHS}$ smaller than $P_{seis,PP}$.
- In the latter case (right panel of Figure 24), $P_{min,UGS/UHS}$ should be kept above $P_{min,PP}$. A reasonable rule of thumb could be to keep $P_{min,UGS/UHS}$ larger than $P_{seis,PP}$.
- If during PP activation occurs on a fault separating two reservoir compartments, during CGI/CCS or UGS/UHS the pressure difference between the adjacent blocks should be safely kept smaller than $P_i - P_{seis,PP}$ (scenario #5b, Figure 16).
- If no activation occurs during PP, $P_{max,CGI/CCS}$ can equate P_i with no particular risk of unexpected events during CGI and UGS. Moreover, ΔP during UGS/UHS can safely span the whole pressure change between P_i and $P_{min,PP}$. In fact, the system operates under reloading conditions and exhibits predominantly elastic behavior within the pressure range that has been previously observed (scenario #4b, Figure 13).

It is crucial to highlight that fault reactivation is largely site-sensitive, depending on the geometry of the fault/reservoir (e.g., the presence of sloped faults, dislocation of the reservoir compartments), differential pore pressure between adjacent reservoir compartments and within each reservoir block, the geomechanical properties of the faults and the reservoir, caprock, under- and over-burden. Therefore, specific investigations are of paramount importance to characterize the actual reservoir setting and quantify more specific bounds.

Moreover, the need of more specific analyses holds in relation to the geochemical effects on fault mechanical properties caused by the substitution of formation fluids with CO_2 , H_2 , or N_2 . In the modeling approach used in this work, these potential effects on faults have only been superficially addressed, due to the lack of laboratory testing.

Finally, we underline that the above rules are aimed at avoiding, or at least limiting, the probability of fault activation. For example, according to [62], “after the onset of fault reactivation, a further pore pressure decline of 3.7 MPa (or 1.6 MPa with no fault offset) and a critically stressed length of approximately 30 m is needed for the nucleation of a seismic event”. Therefore, since fault reactivation can develop with aseismic slip, the recommendations listed above can be considered conservative.

7. Conclusions

Depleted gas reservoirs can serve not only as storage facilities for natural gas (i.e., CH_4) but also for CO_2 , N_2 , and H_2 . The injection and/or withdrawal of these fluids induce changes in the hydraulic and mechanical state of the reservoir. Consequently, deformations and variations in the stress regime develop beneath the subsurface, potentially leading to (seismic/aseismic) reactivation of faults near the reservoir. While the majority of human-induced seismic activities can be associated to injection or withdrawal of fluids at pressures above the original formation pressure causing significant pressure decline [13], which trigger shear stress along faults to reach their limit strength, a few recorded events do not fit this explanation. These seismic events, somehow “unexpected”, develop in reservoirs where:

- seismic events already occurred during the primary production phase;
- in correspondence to a pressure value already experienced by the reservoir during PP.

The main aim of this work has been to understand whether, and under which circumstances, faults can be “unexpectedly” reactivated during USS activities. A one-way quasi-static coupled strategy is adopted to deal with interaction between fluid and the continuous-discontinuous porous formation. The study has been carried out using the typical geological setting of reservoirs located in the Rotliegend formation, in the Netherlands, where systems of almost orthogonal faults split the formation into various compartments. Four underground storage plans, i.e., cyclic storage of CH_4 and H_2 and permanent storage of CO_2 and N_2 , have been investigated. This objective is achieved by analyzing which are the main factors controlling the reactivation of faults under permanent or cyclic storage conditions. The consequences of using different fluids, which affect the pressure evolution over time and the Rotliegend geomechanical properties, have been evaluated.

The simulation of various realistic scenarios have allowed to define the critical factors influencing fault activation during CGI/CCS and UGS/UHS cycles. The stability of the faults bounding the reservoir compartments is mainly jeopardized by an initial stress regime with small horizontal principal components, low friction angle, large pressure change because of injection/withdrawal, and significant contrast between the reservoir and the over-, side-, and underburden stiffness. Concerning faults located between producing blocks, the drivers mainly influencing fault instability are the geometrical setting of the fault/reservoir system, i.e., the offset between reservoir compartments and the fault dip angle, together with the different pressure change in adjacent compartments.

Notice that the pressure recovery and drop addressed in the simulations have been defined based on Dutch regulations, which do not allow the pressure to rise above the initial natural value. Due to this constrain, the mechanisms causing fault reactivation remain similar, irrespective of the fluid considered. The possible mechanical weakening and hardening of the reservoir associated to non-natural pore fluids interaction with the solid grains does not impact significantly the outcomes.

The modeling outcomes have enabled the formulation of general guidelines to define safe operational bandwidths for USS sites, specifically the pressure range over which “unexpected” seismic event can be excluded. These minimum and maximum pressure thresholds are closely linked to the pressures at which seismic events occurred during primary production. The occurrence of a seismic event during PP provides valuable insights for delineating pressure bandwidths within which fault reactivation is highly unlikely during UGS, UHS, CGI, and CCS activities.

These conservative recommendations can serve as a preliminary methodology for reducing the potential risks associated to seismic activity in similar contexts. However, more specific and in-depth evaluations must follow, taking into account the peculiarities of each individual case study.

CRedit authorship contribution statement

Selena Baldan: Investigation, Formal analysis, Writing - original draft. **Massimiliano Ferronato:** Conceptualization, Methodology, Writing - review and editing, Supervision. **Andrea Franceschini:** Methodology, Software, Writing - review and editing. **Carlo Janna:** Software. **Claudia Zoccarato:** Conceptualization, Methodology, Formal analysis, Investigation. **Matteo Frigo:** Software, Investigation. **Giovanni Isotton:** Conceptualization, Methodology, Formal analysis, Software, Funding acquisition. **Cristiano Collettini:** Formal analysis, Writing - review and editing. **Chiara Deangeli:** Methodology, Formal analysis, Writing - review and editing. **Vera Rocca:** Methodology, Formal analysis, Writing - review and editing. **Francesca Verga:** Methodology, Formal analysis, Writing - review and editing. **Pietro Teatini:** Conceptualization, Methodology, Formal analysis, Writing - review and editing, Supervision, Funding acquisition.

Declaration of competing interest

The authors declare that they have no known competing financial interests or personal relationships that could have appeared to influence the work reported in this paper.

Acknowledgements

This research was supported by the State Supervision of Mines (SodM), Ministry of Economic Affairs (The Netherlands), projects KEM01 “Safe Operational Bandwidth of Gas Storage Reservoirs” and KEM39 “Study within the Mining Effects Knowledge Program (KEM-39) on the cyclic storage of gases in the Netherlands”. M.F., A.F., and C.J. from the University of Padova are members of the Gruppo Nazionale Calcolo Scientifico – Istituto Nazionale di Alta Matematica (GNCS-INdAM). Computational resources were provided by University of Padova Strategic Research Infrastructure Grant 2017: “CAPRI: Calcolo ad Alte Prestazioni per la Ricerca e l’Innovazione”.

References

- [1] Al-Shafi, M., Massarweh, O., Abushaikha, A.S., Bicer, Y., 2023. A review on underground gas storage systems: Natural gas, hydrogen and carbon sequestration. *Energy Reports* 9, 6251–6266. doi:10.1016/j.egy.2023.05.236.
- [2] Al-Yaseri, A., Amao, A., Fatah, A., 2023. Experimental investigation of shale/hydrogen geochemical interactions. *Fuel* 346, 128272–128272. doi:10.1016/j.fuel.2023.128272.
- [3] Baisch, S., Koch, C., Voros, R., Rothert, E., 2016. Induced Seismicity in the Bergermeer Field: Hypocenter Relocation and Interpretation. Technical Report. Taqa Energy B.V. TAQA003.
- [4] Bolourinejad, P., Herber, R., 2015. Chemical effects of sulfur dioxide co-injection with carbon dioxide on the reservoir and caprock mineralogy and permeability in depleted gas fields. *Applied Geochemistry* 59, 11–22. doi:10.1016/j.apgeochem.2015.03.003.

- [5] Borello, E.S., Bocchini, S., Chiodoni, A., Coti, C., Fontana, M., Panini, F., Peter, C., Pirri, C.F., Tawil, M., Mantegazzi, A., Marzano, F., Pozzovivo, V., Verga, F., Viberti, D., 2024. Underground hydrogen storage safety: Experimental study of hydrogen diffusion through caprocks. *Energies* 17, 394. doi:10.3390/en17020394.
- [6] Buijze, L., van den Bogert, P.A., Wassing, B.B., Orlic, B., ten Veen, J., 2017. Fault reactivation mechanisms and dynamic rupture modelling of depletion-induced seismic events in a Rotliegend gas reservoir. *Netherlands Journal of Geosciences* 96, s131–s148. doi:10.1017/njg.2017.27.
- [7] Candela, T., Osinga, S., Ampuero, J.P., Wassing, B., Pluymaekers, M., Fokker, P.A., van Wees, J.D., de Waal, H.A., Muntendam-Bos, A.G., 2019. Depletion-induced seismicity at the Groningen gas field: Coulomb rate-and-state models including differential compaction effect. *Journal of Geophysical Research: Solid Earth* 124, 7081–7104. doi:10.1029/2018JB016670.
- [8] Cappa, F., Scuderi, M.M., Collettini, C., Guglielmi, Y., Avouac, J., 2019. Stabilization of fault slip by fluid injection in the laboratory and in situ. *Science Advances* 5. doi:10.1126/sciadv.aau4065.
- [9] Cesca, S., Grigoli, F., Heimann, S., Gonzalez, A., Buforn, E., Maghsoudi, S., Blanch, E., Dahm, T., 2014. The 2013 September-October seismic sequence offshore Spain: a case of seismicity triggered by gas injection? *Geophysical Journal International* 198, 941–953. doi:10.1093/gji/ggu172.
- [10] Collettini, C., Cardellini, C., Chiodini, G., De Paola, N., Holdsworth, R.E., Smith, S., 2008. Fault weakening due to CO₂ degassing in the Northern Apennines: short- and long-term processes. *Geological Society, London, Special Publications* 299, 175–194. doi:10.1144/sp299.11.
- [11] De Jager, J., 2007. Geological development, in: *Geology of the Netherlands*. Royal Netherlands Academy of Arts and Sciences, Amsterdam, pp. 5–26.
- [12] Deflandre, J.P., Laurent, J., Michon, D., Blondin, E., 2018. Microseismic surveying and repeated VSPs for monitoring an underground gas storage reservoir using permanent geophones. *First Break* 13, 129–138. doi:10.3997/1365-2397.1995008.
- [13] Ellsworth, W., 2013. Injection-induced earthquakes. *Science* 341, 1225942–1225942. doi:10.1126/science.1225942.
- [14] Espinoza, D.N., Jung, H., Major, J.D., Sun, Z., Ramos, M.J., Eichhubl, P., Balhoff, M.T., Choens, R.C., Dewers, T.A., 2018. CO₂ charged brines changed rock strength and stiffness at Crystal Geyser, Utah: Implications for leaking subsurface CO₂ storage reservoirs. *International Journal of Greenhouse Gas Control* 73, 16–28. doi:10.1016/j.ijggc.2018.03.017.
- [15] European Commission and Directorate-General for Climate Action, 2019. *Going climate-neutral by 2050 - A strategic long-term vision for a prosperous, modern, competitive and climate-neutral EU economy*. Publications Office. doi:10.2834/02074.
- [16] Foulger, G.R., Wilson, M.P., Gluyas, J.G., Julian, B.R., Davies, R.J., 2018. Global review of human-induced earthquakes. *Earth-Science Reviews* 178, 438–514. doi:10.1016/j.earscirev.2017.07.008.

- [17] Franceschini, A., Baldan, S., Ferronato, M., Janna, C., Zoccarato, C., Frigo, M., Isotton, G., Teatini, P., 2024. Unexpected fault activation in underground gas storage. Part I: Mathematical model and mechanisms. doi:10.48550/arXiv.2308.02198.
- [18] Fuchs, S.J., Espinoza, D.N., Lopano, C.L., Akono, A.T., Werth, C.J., 2019. Geochemical and geomechanical alteration of siliciclastic reservoir rock by supercritical CO₂-saturated brine formed during geological carbon sequestration. *International Journal of Greenhouse Gas Control* 88, 251–260. doi:10.1016/j.ijggc.2019.06.014.
- [19] Gautier, D.L., 2003. Carboniferous-Rotliegend Total Petroleum System Description and Assessment Results Summary. Technical Report. U.S. Geological Survey Bulletin 2211.
- [20] Groenenberg, R.M., Koornnef, J.M., Sijm, J.P.M., Janssen, G.J.M., Morales España, G.A., van Stralen, J., Hernandez-Serna, R., Smekens, K.E.L., Juez-Larre, J., Goncalves Machado, C., Wasch, L.J., Dijkstra, H.E., Wassing, B.B.L., Orlic, B., Brunner, L.G., van der Valk, K., van Unen, M., Hajonides van der Meulen, T.C., Kranenburg-Bruinsma, K.J., Winters, E., Puts, H., van Popering-Verkerk, J., Duijn, M., 2020. Large-Scale Energy Storage in Salt Caverns and Depleted Fields (LSES) - Project Findings. Technical Report. TNO R12006.
- [21] Hager, B.H., Toksoz, M.N., 2009. Technical Review of Bergermeer Seismicity Study TNO Report 2008-U-R1071/B. Technical Report. Massachusetts Institute of Technology.
- [22] Harbert, W., Goodman, A., Spaulding, R., Haljasmaa, I., Crandall, D., Sanguinito, S., Kutchko, B., Tkach, M., Fuchs, S., Werth, C.J., Tsotsis, T., Dalton, L., Jessen, K., Shi, Z., Frailey, S., 2020. CO₂ induced changes in Mount Simon sandstone: Understanding links to post CO₂ injection monitoring, seismicity, and reservoir integrity. *International Journal of Greenhouse Gas Control* 100, 103109. doi:10.1016/j.ijggc.2020.103109.
- [23] Haug, C., Nüchter, J.A., Henk, A., 2018. Assessment of geological factors potentially affecting production-induced seismicity in North German gas fields. *Geomechanics for Energy and the Environment* 16, 15–31. doi:10.1016/j.gete.2018.04.002.
- [24] Heinemann, N., Alcalde, J., M. Miocic, J., T. Hangx, S.J., Kallmeyer, J., Ostertag-Henning, C., Hassanpouryouzband, A., M. Thaysen, E., J. Strobel, G., Schmidt-Hattenberger, C., Edlmann, K., Wilkinson, M., Bentham, M., Haszeldine, R.S., Carbonell, R., Rudloff, A., 2021. Enabling large-scale hydrogen storage in porous media - the scientific challenges. *Energy & Environmental Science* 14, 853–864. doi:10.1039/D0EE03536J.
- [25] Hettema, M.H.H., Schutjens, P.M.T.M., Verboom, B.J.M., Gussinklo, H.J., 2000. Production-induced compaction of a sandstone reservoir: The strong influence of stress path. *SPE Reservoir Evaluation & Engineering* 3, 342–347. doi:10.2118/65410-PA.
- [26] Hu, S., Li, X., Bai, B., Shi, L., Liu, M., Wu, H., 2016. A modified true triaxial apparatus for measuring mechanical properties of sandstone coupled with CO₂-H₂ biphasic fluid. *Greenhouse Gases: Science and Technology* 7, 78–91. doi:10.1002/ghg.1637.
- [27] Hunfeld, L.B., Chen, J., Hol, S., Niemeijer, A.R., Spiers, C.J., 2020. Healing behavior of simulated fault gouges from the Groningen gas field and implications for induced fault reactivation. *Journal of Geophysical Research: Solid Earth* 125, e2019JB018790. doi:10.1029/2019JB018790.

- [28] Hunfeld, L.B., Niemeijer, A.R., Spiers, C.J., 2017. Frictional properties of simulated fault gouges from the seismogenic Groningen gas field under in situ P–T-chemical conditions. *Journal of Geophysical Research: Solid Earth* 122, 8969–8989. doi:10.1002/2017JB014876.
- [29] Isotton, G., Teatini, P., Ferronato, M., Janna, C., Spiezia, N., Mantica, S., Volonte, G., 2019. Robust numerical implementation of a 3D rate-dependent model for reservoir geomechanical simulations. *International Journal for Numerical and Analytical Methods in Geomechanics* 43, 2752–2771. doi:10.1002/nag.3000.
- [30] Jiang, G., Liu, L., Barbour, A.J., Lu, R., Yang, H., 2021. Physics-based evaluation of the maximum magnitude of potential earthquakes induced by the Hutubi (China) underground gas storage. *Journal of Geophysical Research: Solid Earth* 126, e2020JB021379. doi:10.1029/2020JB021379.
- [31] Keranen, K.M., Weingarten, M., 2018. Induced seismicity. *Annual Review of Earth and Planetary Sciences* 46, 149–174. doi:10.1146/annurev-earth-082517-010054.
- [32] Kim, K., Makhnenko, R.Y., 2022. Short- and long-term responses of reservoir rock induced by CO₂ injection. *Rock Mechanics and Rock Engineering* 55, 6605–6625. doi:10.1007/s00603-022-03032-1.
- [33] Kraaijpoel, D., Nieuwland, D., Dost, B., 2013. Microseismic monitoring and subseismic fault detection in an underground gas storage, in: *Proc. 4th EAGE Passive Seismic Workshop*, Amsterdam, Netherlands, European Association of Geoscientists & Engineers. pp. 1–3. doi:10.3997/2214-4609.20142354.
- [34] Liu, C., Zhang, F., Wang, Q., Wang, B., Zhang, Q., Xu, B., 2023. Evaluation of fault stability and seismic potential for Hutubi underground gas storage due to seasonal injection and extraction. *Underground Space* 13, 74–85. doi:10.1016/j.undsp.2023.03.006.
- [35] Marbler, H., Erickson, K.P., Schmidt, M., Lempp, C., Pöllmann, H., 2012. Geomechanical and geochemical effects on sandstones caused by the reaction with supercritical CO₂: an experimental approach to in situ conditions in deep geological reservoirs. *Environmental Earth Sciences* 69, 1981–1998. doi:10.1007/s12665-012-2033-0.
- [36] Mikhaltsevitch, V., Lebedev, M., Gurevich, B., 2014. Measurements of the elastic and anelastic properties of sandstone flooded with supercritical CO₂. *Geophysical Prospecting* 62, 1266–1277. doi:10.1111/1365-2478.12181.
- [37] Ministry of Economic Affairs and Climate Policy, 2021. Natural resources and geothermal energy in the Netherlands - Annual review 2020. URL: https://www.nlog.nl/sites/default/files/2021-06/pre-publ_ch4_yearbook2020_en.pdf.
- [38] Miocic, J., Heinemann, N., Edlmann, K., Scafidi, J., Molaei, F., Alcalde, J., 2023. Underground hydrogen storage: a review. *Geological Society, London, Special Publications* 528, 73–86. doi:10.1144/SP528-2022-88.
- [39] Muntendam-Bos, A.G., Hoedeman, G., Polychronopoulou, K., Draganov, D., Weemstra, C., van der Zee, W., Bakker, R.R., Roest, H., 2022. An overview of induced seismicity in the Netherlands. *Netherlands Journal of Geosciences* 101, e1. doi:10.1017/njg.2021.14.

- [40] Muntendam-Bos, A.G., Roest, J.P.A., de Waal, J.A., 2015. A guideline for assessing seismic risk induced by gas extraction in the Netherlands. *The Leading Edge* 34, 672–677. doi:10.1190/tle34060672.1.
- [41] Nederlandse Aardolie Maatschappij BV, 2016. Norg UGS fault reactivation study and implications for seismic threat. Technical Report. NAM EP201610208045.
- [42] Peter, A., Yang, D., Eshiet, K.I.I.I., Sheng, Y., 2022. A review of the studies on CO₂-brine-rock interaction in geological storage process. *Geosciences* 12, 168. doi:10.3390/geosciences12040168.
- [43] Porthos CO₂ Transport and Storage C.V., 2024. CO₂ reduction through storage under the North Sea. <https://www.porthosco2.nl/en>. Accessed: 2024-09-03.
- [44] Rasmussen, A., Sandve, T., Bao, K., Lauser, A., Hove, J., Skaflestad, B., Klöfkorn, R., Blatt, M., Rustad, A., Sæ vareid, O., Lie, K., Thune, A., 2021. The Open Porous Media Flow reservoir simulator. *Computers & Mathematics with Applications* 81, 159–185. doi:10.1016/j.camwa.2020.05.014.
- [45] Rimmelé, G., Barlet-Gouédard, V., Renard, F., 2010. Evolution of the petrophysical and mineralogical properties of two reservoir rocks under thermodynamic conditions relevant for CO₂ geological storage at 3 km depth. *Oil & Gas Science and Technology - Revue de l'Institut Français du Pétrole* 65, 565–580. doi:10.2516/ogst/2009071.
- [46] Rohmer, J., Pluymakers, A., Renard, F., 2016. Mechano-chemical interactions in sedimentary rocks in the context of CO₂ storage: Weak acid, weak effects? *Earth-Science Reviews* 157, 86–110. doi:10.1016/j.earscirev.2016.03.009.
- [47] Samuelson, J., Spiers, C.J., 2012. Fault friction and slip stability not affected by CO₂ storage: Evidence from short-term laboratory experiments on North Sea reservoir sandstones and caprocks. *International Journal of Greenhouse Gas Control* 11, S78–S90. doi:10.1016/j.ijggc.2012.09.018.
- [48] Schlumberger, 2014. ECLIPSE Industry Reference Reservoir Simulator. URL: <https://www.software.slb.com/products/eclipse>.
- [49] Segall, P., Grasso, J.R., Mossop, A., 1994. Poroelastic stressing and induced seismicity near the Lacq gas field, southwestern France. *Journal of Geophysical Research: Solid Earth* 99, 15423–15438. doi:10.1029/94JB00989.
- [50] Shoushtari, S., Namdar, H., Jafari, A., 2023. Utilization of CO₂ and N₂ as cushion gas in underground gas storage process: A review. *Journal of Energy Storage* 67, 107596. doi:10.1016/j.est.2023.107596.
- [51] Teatini, P., Ferronato, M., Franceschini, A., Frigo, M., Janna, C., Zoccarato, C., 2019. Gas storage in compartmentalized reservoirs: a numerical investigation on possible “unexpected” fault activation, in: 53rd US Rock Mechanics / Geomechanics Symposium, Paper #ARMA 19-1991, American Rock Mechanics Association. pp. 1–9.
- [52] Teatini, P., Zoccarato, C., Ferronato, M., Franceschini, A., Frigo, M., Janna, C., Isotton, G., 2020. About geomechanical safety for UGS activities in faulted reservoirs. *Proceedings of the International Association of Hydrological Sciences* 382, 539–545. doi:10.5194/piahs-382-539-2020.

- [53] The Open Porous Media Initiative, 2023. Open Porous Media. <https://opm-project.org>. Accessed: 2024-09-03.
- [54] TNO, 2015. Injection-Related Induced Seismicity and its Relevance to Nitrogen Injection: Description of Dutch Field Cases. Technical Report. TNO R10906.
- [55] Uta, P., 2017. Recent Intraplate Earthquakes in Northwest Germany - Glacial Isostatic Adjustment and/or a Consequence of Hydrocarbon Production. Ph.D. thesis. Leibniz University Hannover. doi:10.15488/9088.
- [56] Van Hulten, F.F.N., 2010. Geological factors effecting compartmentalization of Rotliegend gas fields in the Netherlands, in: Reservoir Compartmentalization. Geological Society of London, pp. 301–315. doi:10.1144/SP347.17.
- [57] Van Wees, J., Buijze, L., Thienen-Visser, K., Nepveu, M., Wassing, B., Orlic, B., Fokker, P., 2014. Geomechanics response and induced seismicity during gas field depletion in the Netherlands. *Geothermics* 52, 206–219. doi:10.1016/j.geothermics.2014.05.004.
- [58] Vasile, N.S., Bellini, R., Bassani, I., Vizzarro, A., Azim, A.A., Coti, C., Barbieri, D., Scapolo, M., Viberti, D., Verga, F., Pirri, F., Menin, B., 2024. Innovative high pressure/high temperature, multi-sensing bioreactors system for microbial risk assessment in underground hydrogen storage. *International Journal of Hydrogen Energy* 51, 41–50. doi:10.1016/j.ijhydene.2023.10.245.
- [59] Verga, F., 2018. What’s conventional and what’s special in a reservoir study for underground gas storage. *Energies* 11, 1245. doi:10.3390/en11051245.
- [60] Vilarrasa, V., De Simone, S., Carrera, J., Villaseñor, A., 2021. Unraveling the causes of the seismicity induced by underground gas storage at Castor, Spain. *Geophysical Research Letters* 48, e2020GL092038. doi:10.1029/2020GL092038.
- [61] Walsh, F.R., Zoback, M.D., 2016. Probabilistic assessment of potential fault slip related to injection-induced earthquakes: Application to north-central Oklahoma, USA. *Geology* 44, 991–994. doi:10.1130/g38275.1.
- [62] Wassing, B.B.T., Buijze, L., Ter Heege, J.H., Orlic, B., Osinga, S., 2017. The impact of viscoelastic caprock on fault reactivation and fault rupture in producing gas fields, in: U.S. Rock Mechanics/Geomechanics Symposium. Paper #ARMA-2017-0355, American Rock Mechanics Association.
- [63] Zhou, P., Yang, H., Wang, B., Zhuang, J., 2017. Seismological investigations of induced earthquakes near the Hutubi underground gas storage facility. *Journal of Geophysical Research: Solid Earth* 124, 8753–8770. doi:10.1029/2019JB017360.